AMERICAN UNIVERSITY OF BEIRUT

TUNABLE NEAR-FIELD HEAT TRANSFER WITH PIEZOELECTRIC MATERIALS

by
RAZAN IBRAHIM BALTAJI

A thesis
submitted in partial fulfillment of the requirements
for the degree of Master of Science
to the Department of Physics
of the Faculty of Arts and Sciences
at the American University of Beirut

Beirut, Lebanon
August 2018

AMERICAN UNIVERSITY OF BEIRUT

TUNABLE NEAR-FIELD HEAT TRANSFER WITH PIEZOELECTRIC MATERIALS
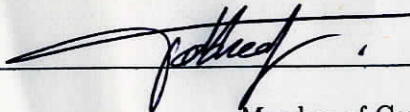
by
RAZAN IBRAHIM BALTAJI

Approved by:

_____

Dr. Michel Kazan, Professor   Advisor
Physics

_____

Dr. Mounib Eid, Professor   Member of Committee
Physics

_____

Dr. Malek Tabbal, Professor   Member of Committee
Physics

Date of thesis defense: August 24, 2018

AMERICAN UNIVERSITY OF BEIRUT

THESIS, DISSERTATION, PROJECT RELEASE FORM

Student Name: _Battaji_ _Razan_ _Ibrahim_
Last   First   Middle

☑ Master's Thesis   ○ Master's Project   ○ Doctoral Dissertation

☑ I authorize the American University of Beirut to: (a) reproduce hard or electronic copies of my thesis, dissertation, or project; (b) include such copies in the archives and digital repositories of the University; and (c) make freely available such copies to third parties for research or educational purposes.

☐ I authorize the American University of Beirut, to: (a) reproduce hard or electronic copies of it; (b) include such copies in the archives and digital repositories of the University; and (c) make freely available such copies to third parties for research or educational purposes after: **One** ___ year from the date of submission of my thesis, dissertation or project.
Two ___ years from the date of submission of my thesis, dissertation or project.
Three ___ years from the date of submission of my thesis, dissertation or project.

_____   _Aug 31, 2019_
Signature   Date

This form is signed when submitting the thesis, dissertation, or project to the University Libraries

Acknowledgements

To my Abdurrahman.

An Abstract of the Thesis of

Razan Ibrahim Baltaji   for   Master of Science

Major: Physics

Title: Tunable Near-Field Heat Transfer with Piezoelectric Materials

Realizing a thermal counterpart for electronic devices has been recently proposed; a thermal analogue requires processing information by heat currents rather than by electric currents. Phononic heat currents are fundamentally limited by the speed of acoustic phonons smaller than the speed of electrons by orders of magnitude alongside the reduction of heat flow by local Kapitza resistances arising from the mismatch of vibrational modes at interfaces. Overlooked due to the relatively weak heat flux limited by the Stefan-Boltzmann law in the far-field limit, energy transfer mediated by thermal photons with contactless devices in the near-field limit (NFRHT) has been recently considered as an alternative.

Several approaches for heat transfer modulation have been applied exploiting the dependence of NFRHT on the geometric asymmetry of the surfaces, the material properties, and the relative motion of the radiating objects. Classes of materials studied include phase-change materials (PCM), ferroelectrics, and chiral materials. In this dissertation, we propose, to the best of our knowledge, for the first time the use of piezoelectrics for near-field radiative transfer modulation. We detect a phase change in the optical properties of oxygen-contaminated AlN attributed to an Oxygen related defect. The piezoelectric properties of AlN enables fast electrical tuning and thus modulation of NFRHT. We show that radiative heat transfer between the two piezoelectric materials can be tuned as much as 40% by switching between the two phases. In addition, we detect a coherence shift in near field transfer corresponding to the two phases of AlN and demonstrate coherence tuning by a factor of 3.7.

We investigate the near-field radiative heat transfer between both the parallel plates and the two sphere geometries. We demonstrate for the first time modulation of NFRHT in the two sphere system via harnessing phase change in the dielectric properties of the emitters material. We adopt the model proposed by Narayanaswamy and Gang for calculating the NFRHT spectral conductivity be-

tween two spheres applicable for arbitrary sphere sizes. We highlight the distinct properties of the near-field transfer along with the distinct resonance conditions for the two spheres geometry looking for asymptotic regimes for optimizing near-field thermal transfer modulation.

Contents

List of Figures

Nomenclature

$\hat{\varepsilon}$ electric permittivity

μ_0 magnetic permeability of free space

ϕ_e electric scalar potential

ρ_e electric charge density

σ electric conductivity

$\mathbf{I}$ identity dyad

Θ mean energy of a Planck oscillator at thermal equilibrium at temperature T

ε complex electric permittivity

ε_r relative permittivity or dielectric function

$\vec{A}$ magnetic vector potential

$\vec{J^r}$ random current density

D spectral mode density

$e_{b,\lambda}$ Blackbody spectral emissive power

$e_{b,\omega}$ spectral emissive power

k wavevector

n mode occupation number of photons at thermal equilibrium

u^0 spectral energy density

1

Chapter 1

Introduction

1.1 Electromagnetic Fluctuations at the Nanoscale

The study of electromagnetic fluctuations at the nanoscale is essential for modern applied science. In the fluctuational electrodynamics framework, nanoscale electromagnetic fluctuations are described by introducing a 'random' field into Maxwell's equations offering a theoretical framework for modeling various interactions such as Van der Waal's and Casimir forces, radiative heat transfer, Casimir friction, electromagnetic trapping mechanisms, as well as a number of major physiochemical phenomena near the surface of condensed media. In particular, fluctuational electrodynamics, as we thoroughly investigate, offers the theoretical framework for modeling radiative heat transfer in the *near-field* regime where traditional formulations of thermal radiation cease to be valid.

Similar to radiative heat transfer, deviation from classical conductive heat transfer formulations such as the Fourier conduction law has been well established for small length scales. However, the violation of Planck's law, as the classical formulation for radiative heat transfer, and therefore the blackbody limit, which
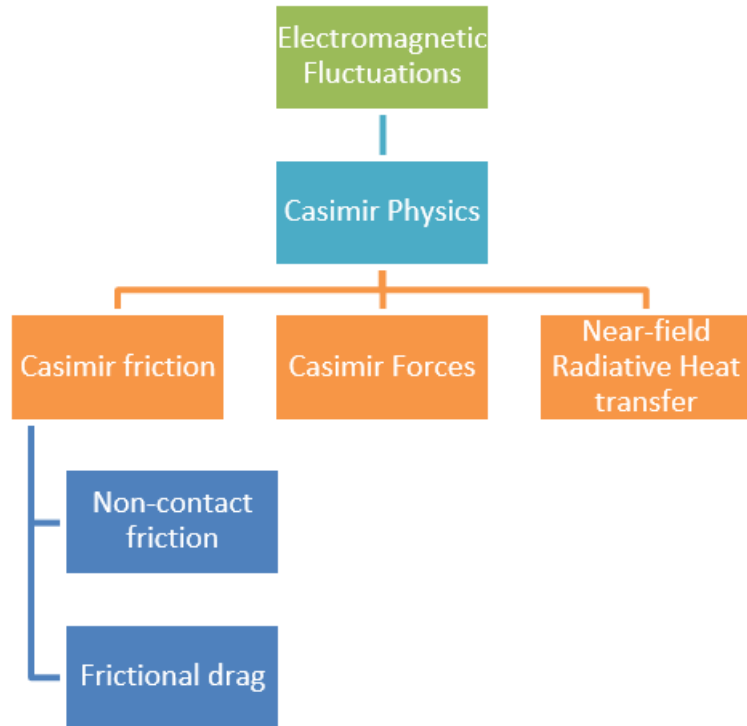
Figure 1.1: *Nanoscale Fluctuational Electrodynamics Physics*

has set a maximum for heat transfer for a long time, has been recently demonstrated theoretically and experimentally. In contrary to classical formulations regarding thermal radiation as incoherent, partially temporally and spatially coherent thermal radiation has been detected. Astoundingly, thermal transfer has been detected exceeding the blackbody limit especially in the presence of surface electromagnetic waves up to several orders of magnitude. Thus a new era in harnessing radiative heat transfer at the nanoscale has been initiated opening up novel unprecedented applications. This deviation from the classical theory, as investigated in Chapter 3, is due to the *near-field* effects described in terms of electromagnetic fluctuations dominating heat transfer when the dimensions of the objects and/or the gap separation is less than the peak thermal wavelength [].

1.2 Classical Formulations of Radiative Heat Transfer

The relation between temperature and thermal radiation emitted by objects pre-occupied 19th century physicists. Introducing his bold assumption of the quanta of energy in contrary to classical electrodynamics, Max Planck used the maximum entropy principle, to derive *Planck's law* quantifying the spectral emissive power of blackbodies in agreement with *Wien's formula*, applicable to the short-wavelength region of the blackbody spectrum, and the *Rayleigh-Jeans formula*, applicable for sufficiently high temperatures and long wavelengths. Planck's law of blackbody thermal radiation describes spectral emissive power of a blackbody $e_{b,\lambda}$ in a cavity in thermal equilibrium as [1]

$$e_{b,\lambda} = \frac{2\pi h c^2}{\lambda^5 (e^{hc/k_B \lambda T} - 1)} \tag{1.1}$$

Since then, Planck's law has been of fundamental importance to the study of radiative heat transport and thermal radiation of isolated objects. Thermal emission from real materials can be described by comparison with that emitted by a blackbody at the same temperature using a property called *emissivity*. The wavelength at which the spectral emissive power is maximum is given by

$$\lambda_W \approx \frac{2900}{T} \mu m \tag{1.2}$$

This relationship is historically called the *Wien's displacement law*. At room temperature ($\sim 300K$), the peak wavelength is about $10\mu m$. The total emissive power of a blackbody is thus given by $e_b = \sigma T^4$ as predicted by *Stefan-Boltzmann law*. For a real object the spectral emissive power is given by $e_b = \varepsilon_\lambda e_{b,\lambda}$ where
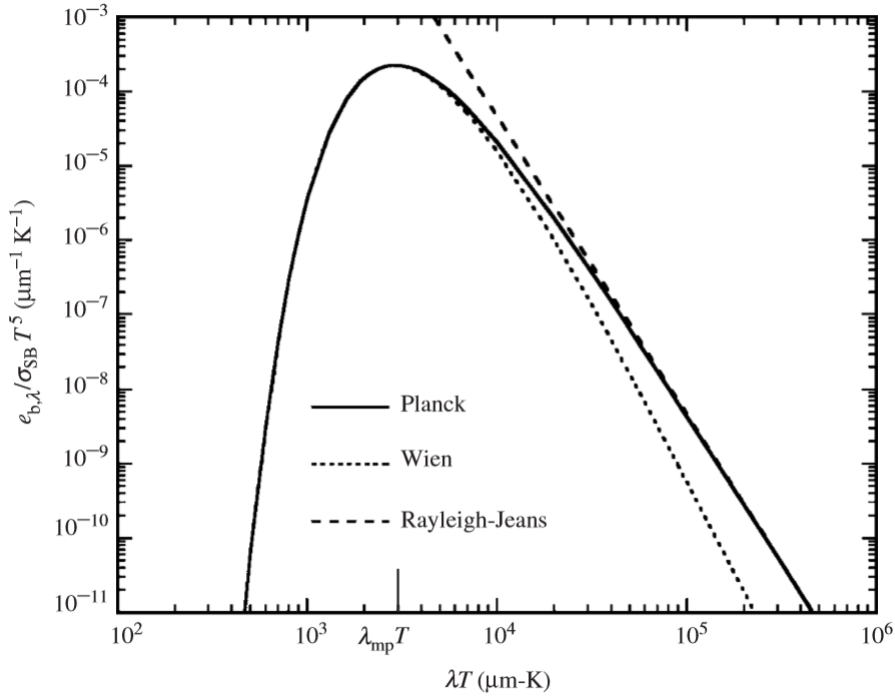
Figure 1.2: *Planck's Law for Blackbody emissive power*

ε_λ is its emissivity at a wavelength of λ and $\varepsilon_\lambda \in [0, 1]$. Accordingly, the Stefan-Boltzmann law has set the maximum emissive power, referred to as the *blackbody limit*, that is possible for any object, at a temperature T.

1.3   An Overview of Near-field Radiative Heat Transfer

The quantum mechanical formulation of Rytov's fluctuational electrodynamics around the early 1950s [2], allowed for the first time relating thermal radiation to its origin in the random fluctuations of charges acting as a stochastic current source for thermal radiation. Thermally excited electromagnetic waves, as later expanded upon in chapter 2, are of two types: propagating waves that radiate
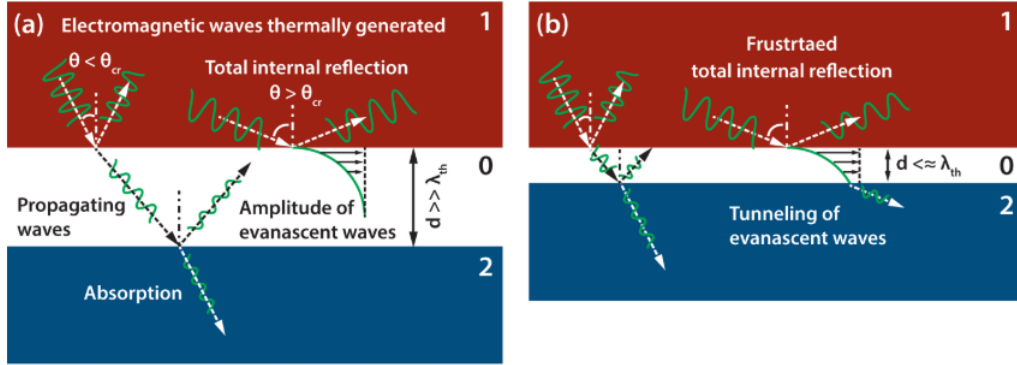
Figure 1.3: *(a) Schematic for far-field radiation between two parallel semi-infinite bodies (b) Schematic for near-field radiation for a vacuum gap comparable to or smaller than the peak thermal wavelength*

into free space, and non-propagating (evanescent) waves that decay away from the surface on one or both sides of the surface of the emitter. Since the non-propagating waves decay away from the emitter surface, no transport of energy in a non-absorbing medium occurs unless another object is brought close enough to the emitter, resulting in the *tunneling* of non-propagating waves as demonstrated in Fig. 1.3. The tunneling of non-propagating waves is the key to the enhanced energy transfer in the near field limit.

The classical theory of blackbody radiation, as proposed by Planck deals only with the propagating modes and thus is only applicable when evanescent waves can be ignored. The non-propagating modes are unimportant only when the characteristic linear dimensions and gap between objects participating in thermal radiative transfer are larger than the peak thermal wavelength, thus what is called the *far-field* regime, which is approximately $10\mu m$ at room temperature [3]. However, when the size of the bodies and/or their separation distance is comparable to or smaller than the thermal wavelength, Planck's theory ceases to be valid and radiation heat transfer is said to be in the *near-field* regime and is described by the fluctuational electrodynamics formulation for thermal radiation.

6

1.4   Purpose and outline

The control of electric currents in solids is at the cornerstone of modern electronics. The diode and transistor are the fundamental building blocks of modern electronic technologies, allowing for rectifying, switching, modulating, and amplifying electric currents. The thermal analogue for electronic systems would exhibit faster responses, and consequently would pave the way for new generation of technological applications. Therefore, much attention has been directed toward thermal structures for rectifying, switching, modulating and amplifying heat flux. Purely phononic systems have been proposed [4, 5, 6]; however, phononic heat transfer suffers from some weaknesses of fundamental nature which intrinsically limit its performance [6]. One limitation is linked to the speed of acoustic phonons which is limited by the speed of sound in solids. Another limitation is the presence of local Kapitza resistances which is a result of the acoustic and vibrational mismatch that may arise between different solid elements in contact. This resistance can drastically reduce the heat flux transported across the system [7]. Therefore, an alternative for phononic heat transfer is required for a thermal analogue of for electronic systems.

Because of the much lower heat flux limited by the Stefan-Boltzmann law in comparison to other heat transfer modes, thermal radiation was not traditionally considered as an effective means for thermal management. Nevertheless, with the significant enhancement by orders of magnitude demonstrated in the near-field limit, near-field radiative heat transfer (NFRHT) has shown great potential in controlling heat flow at the nanoscale. The capability of modulating heat flow with near-field radiative transport can help realizing a photonic alternative to the phononic systems.

Recent works have theoretically proposed photonic systems operating via NFRHT such as: thermal transistors [8], thermal rectifiers [9], photonic thermal logic gates [10], and thermal memory [11] as an analog for electronic systems. To achieve the functions of the proposed systems, tuning and modulating NFRHT is crucial. Several approaches have been proposed to modulate radiative heat transfer. One scheme exploits the dependence of NFRHT on the geometric asymmetry of the surfaces or objects. For example modulation of NFRHT by changing the relative orientation between gratings [12] and cylinders [13] has been theoretically predicted. Another approach for modulating NFRHT is based on dynamic non-equilibrium by changing the relative movement between the radiating objects where the Doppler effect resulting from the motion modifies the reflection coefficient, thus, modulating heat transfer [14, 15]. Furthermore, a major scheme for modulating the near-field heat transfer is by tuning optical properties of materials. Modulation can be fast if tuning can be done via an electric or a magnetic field.

Classes of materials investigated for modulating NFRHT so far include: phase-change materials (PCM), ferroelectrics, and chiral materials. Modulating NFRHT was proposed for chiral materials with magnetoelectric coupling via ultrafast optical pulses [16] and for ferroelectric materials via an external electric field [17]. Borrowing from research on modulating Casimir force, PCMs such as AIST [18] and Vanadium Dioxide (VO_2) [19] has been proposed for modulating NFRHT. Both can be switched between an amorphous and a crystalline state with a switching time on the order of a few nanoseconds by changing the lattice parameters via temperature. Although these materials showed efficient thermal modulation, they are limited to applications in which the temperature does not exceed the phase change temperature. In this work, we demonstrate that defect complexes

8

in aluminum nitride AlN give rise to soft phonon modes that depend on the lattice parameter and can be used for near-field thermal radiation modulation. We hope that our results will open the door for new applications of near-field thermal radiations as AlN has an important advantage over the commonly known phase change materials that its lattice parameters can be changed by the application of an electric field because of its high piezoelectric properties irrespective of the ambient temperature.

Most of the research on tuning NFRHT for thermal modulation focus on semi-infinite plates geometry [16, 17, 18, 19]. However, other geometries remain poorly studied. For instance, the two sphere geometry has an additional length parameter for heat transfer as well as surface polariton resonance conditions specific for the spherical geometry, thus leading to novel properties for near-field heat transfer modulation. Thermal rectification for the two sphere system geometry has been proposed in Ref. [20] providing distinctive properties for thermal rectification in contrary to the typical parallel plate system. The scale invariance properties of the resonance modes of the spheres has shown to result in a large difference in the coupling constants between relevant modes in the forward and reverse scenarios, thus, providing a mechanism for thermal rectification [20]. NFRHT modulation in the two nanoparticles system has been simulated for anisotropic particles by controlling their orientations [21]. However to the best of our knowledge, tuning and modulating NFRHT by harnessing the properties of phase changing materials has not yet been applied to the two sphere system.

This dissertation is organized as follows. After the introduction, we present in Chapter 2 low temperature reflectivity measurements highlighting the detected defect state change in AlN. We also introduce the Kramers-Kronig analysis technique for calculating the dielectric function for both defect states of AlN start-

ing from the reflectivity measurements. In addition, we introduce the surface phonon polaritons localized waves in both states, which are strongly related to the infrared dielectric function and are the principle determinant of the near-field radiation characteristics and the key players in tuning NFRHT. We also demonstrate the resonance conditions for both the parallel plates and the two sphere geometries highlighting the contrast between the two states of AlN. In chapter 3, we introduce the fundamentals of near-field radiative transfer concluding with the NFRHT for the semi-infinite plates geometry. We investigate the near-field transfer between two AlN plates harnessing the defect state change in AlN for near-field thermal modulation and coherence tuning. In chapter 4, we introduce the adopted Narayanaswamy model [22] for computing NFRHT for the two sphere geometry investigating near-field transfer modulation and coherence tuning between two AlN spheres. Finally, we conclude with the limitations of our study and an outlook for future and current research.

Chapter 2

Infrared Spectrum of Oxygen Contaminated Aluminum Nitride

2.1 Oxygen-related Defect in Aluminum Nitride

Oxygen-related defect complexes have always been considered as the most important native defects in AlN ceramics, and the local atomic structure of oxygen point defect has been intensively investigated [23, 24]. Theories have shown that oxygen acts as a deep center in the wide band gap of AlN and substitutes for the nitrogen atom in several charge states. Experiments demonstrated that a change in the nature of the oxygen defect occurs above a critical value of oxygen concentration [25, 26]. The model that has been proposed suggests that, at concentration below 0.75%, the oxygen substitutes for nitrogen in the lattice, with one aluminum vacancy occurring for every three substituted oxygen atoms. However, for a concentration greater than 0.75% a new type of defect is stable, in which an aluminum atom is octahedrally bound to an increasing number of oxygen atoms. No oxygen substitution for aluminum in the lattice has been

reported.

Infrared spectroscopy can detect the oxygen-related defect complexes through their localized and extended vibrational modes. We present below a simple theory about the effect of defect formation on the lattice dynamics. This theory will show that a change in the oxygen accommodation results in the oxygen-related defect complexes modes frequency, and consequently a change in the infrared spectrum.

The general equations for the vibrations of a perfect (Bravais) lattice take the form:

$$M_s \nu^2 U_{sl} - \sum_{s'l'} G_{ss'll'} U_{s'l'} = 0 \tag{2.1}$$

where M_s is the atomic mass of the atom on the site s, U_{sl} and $U_{s'l'}$ are the displacement vector elements of the atom on the site s of the cell l and that on the site s' of the cell l', respectively, and $G_{ss'll'}$ denotes the interatomic forces.

If we suppose now that we have made a change δM in the mass of the atom at $l = 0$, **at?** an arbitrary site, and/or some change $\delta G_{ss'll'}$ in the interactions of this atom with its neighbors in the crystal. Our dynamical equations in (2.1) would now be read

$$M_s \nu^2 U_{sl} - \sum_{s'l'} G_{ss'll'} \cdot U_{s'l'} + \delta M \nu^2 U_0 + \sum_{s'l'} \delta G_{ss'll'} \cdot U_{s'l'} = 0 \tag{2.2}$$

which we symbolize as

$$LU + \delta LU = 0 \tag{2.3}$$

and therefore

$$(1 + R\delta L)U = 0 \tag{2.4}$$

where the resolvent or Green function, R, is the matrix inverse of the dynamical matrix L. If R exists and can be calculated, we are on the way to solving the

linear equations symbolized by (2.4). The resolvent must be a function of ν^2, satisfying the abstract formula

$$R(\nu^2) \cdot L(\nu^2) = 1 \tag{2.5}$$

If we take the displacement vectors to be

$$U_l = U_q \exp(iql) \tag{2.6}$$

where q denotes a phonon wave vector. Using the standard orthogonality properties of the solutions of (2.1), we find that the matrix $R(\nu^2)$ may be expressed in the form

$$R_{ll'} = \frac{1}{NM} \sum_q \frac{U_q^* U_q}{\nu^2 - \nu_q^2} \exp[iq(l - l')] \tag{2.7}$$

where N is the number of cells in the crystal. Here, for simplicity, we suppose that the sum over all wave vectors q is extended to include the various modes of phonon polarization.

Consider now an impurity where there is only a change in mass in (2.2). Substituting from (2.7) into (2.2), we get an equation involving only U_0, the displacement vector on this site. This contains only the sum for $R_{00}(\nu^2)$, i.e.

$$\left[1 + \frac{\delta M}{M} \frac{\nu^2}{N} \sum_q \frac{U_q^* U_q}{\nu - \nu^2} \right] \cdot U_0 = 0 \tag{2.8}$$

To understand what happens, when an impurity substitutes for an atom in the lattice, let us ignore geometrical features such as the vector character of U_0 and treat (2.8) as a scalar equation. The normal mode frequencies are therefore roots

13

of an equation of the form

$$1 + \frac{\delta M}{M} \frac{1}{N} \sum_q \frac{\nu^2}{\nu^2 - \nu_q^2} = 0 \qquad (2.9)$$

If we look for points where the function

$$f(\nu^2) = \frac{1}{N} \sum_q \frac{\nu^2}{\nu^2 - \nu_q^2} \qquad (2.10)$$

intersects the horizontal line (independent of ν) at $\frac{-M}{\delta M}$, we can distinguish two cases:

Suppose first that δM is negative. Each root of (2.1) must lie above a pole of $f(\nu^2)$; the normal modes of the perturbed system are interleaved in frequency between those of the perfect crystal. Since the values of ν_q form a dense band, whose spacing tends to zero like $1/N$, most of the new solutions are indistinguishable from the old. However, the higher root is not constrained, but can move away from the top of the band by a finite amount. This mode must be localized. It follows that, when δM is negative, the reflectivity spectrum will exhibit a two-mode behavior and an additional band must be observed.

In contrast to this, for the case when δM is positive, the substituted impurity ion must give rise either to a localized gap mode between the acoustical and optical branches of the host crystal, or to in-band resonance mode where the amplitude of vibration is much larger at the impurity site than in the rest of the crystal, but does not die away exponentially with distance and is therefore not strictly localized. Indeed, this would result in IR spectrum distortion. Thus, when an in-band resonance mode occurs, the reflectivity spectrum exhibits only one distorted Reststrahlen band.

14

The temperature dependent FTIR spectra are shown in Fig 2.1. One criterion for in-gap localized mode and consequently two-mode behavior is that the phonon dispersion of the host crystal be such that a gap does exist between its acoustical and optical branches. In other words, the density of phonon states must be very low between the acoustical and optical branches. AlN in its wurtzite structure does not have such a gap, and it therefore follows that any impurity with an atomic mass larger than that of nitrogen (δM positive) that substitutes for nitrogen cannot exhibit the conventional two-mode behavior. Therefore, strict one-mode behavior is possible when an oxygen impurity (which has a larger atomic mass than that of nitrogen) substitutes for nitrogen. Thus, we attribute the weak peaks below the lower edge of the main reststrahlen band to in-band resonance modes caused by nitrogen vacancy substituted by oxygen as highlighted in Fig. 2.2. However, these peaks present drastic changes in their intensities when the temperature reaches 90 K. This can be interpreted as a change in the oxygen accommodation when the AlN unit cell expands above a certain threshold corresponding to a temperature of 90 K.

The fact that AlN is a good piezoelectric material allows the control of the expansion and compression of the AlN unit cell, and consequently the oxygen-related defect complex formation, using an electric field with keeping the temperature of the material around any fixed temperature. In other words, oxygen defect state transition in AlN can be controlled using an electric field without changing the sample temperature.
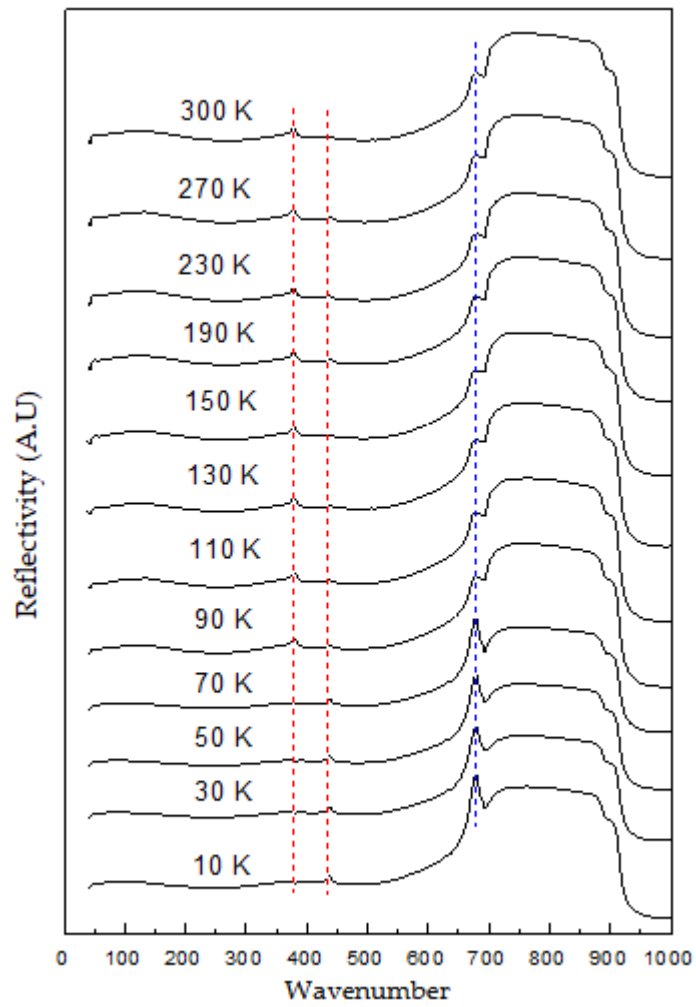
Figure 2.1: *Low Temperature Reflectivity measurements. The dashed vertical lines are used to help tracking the transition of a localized defect mode into an in-band resonant mode indicating a change in defect state*

16
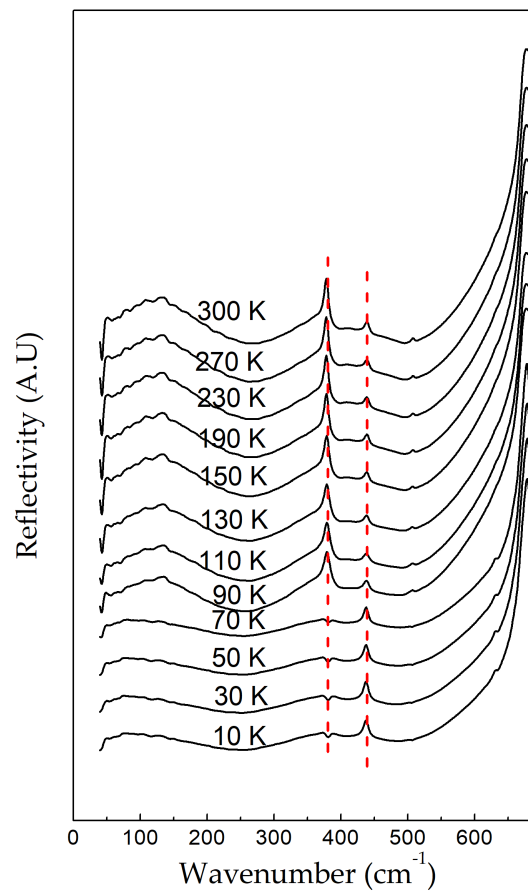
Figure 2.2: *Low Temperature Reflectivity measurements*

2.2   Kramers– Kronig Conversion Technique

2.2.1   Relationship between the complex dielectric function and reflectivity

The reflectivity spectra obtained by FTIR measurement can be described by Fresnel equations of reflectivity. The Fresnel coefficient of reflectivity is defined as the ratio of reflected electric field (E_r) to incident electric field (E_i) and is related to the complex response function in the following way

$$r(\omega) = \frac{E_r}{E_i} = \frac{\sqrt{\varepsilon(\omega)} - 1}{\sqrt{\varepsilon(\omega)} + 1} \tag{2.11}$$

The Fresnel coefficient of reflectivity is a complex function itself which can be written as

$$r(\omega) = \rho(\omega)e^{i\theta(\omega)} \tag{2.12}$$

where $\rho(\omega)$ is the amplitude and $\theta(\omega)$ is the phase. The quantity being measured is the reflectivity which is defined as the complex conjugate of the Fresnel coefficient of reflectivity

$$R(\omega) = rr^* = \rho(\omega)^2 \tag{2.13}$$

Unlike the amplitude $\rho(\omega)$ which is a real quantity, the phase $\theta(\omega)$ cannot be directly measured because it is an imaginary quantity. However it is possible to determine $\theta(\omega)$ using a Kramers– Kronig conversion technique if the reflectivity $R(\omega)$ is known for all frequencies.

2.2.2 Kramers–Kronig Relations

The Kramers–Kronig conversion technique is a mathematical tool that allows the evaluation of the real part of the dielectric function if the imaginary part is known for all frequencies and vice versa. In order to apply the Kramers–Kronig relations, a function must satisfy the following conditions:

1. The poles of $\varepsilon(\omega)$ must be below the real axis.

2. The integral of $\varepsilon(\omega)/\omega$ taken over an infinite semi- circle in the upper region of the complex plane must tend to zero. In other words, $\varepsilon(\omega) \to 0$ as $|\omega| \to \infty$.

3. The real part $\varepsilon_1(\omega)$ should be an even function while the imaginary part $\varepsilon_2(\omega)$ an odd function with respect to the real variable ω.

We consider now the following Cauchy integral:

$$\varepsilon(\omega) = \frac{1}{i\pi} P \int_{-\infty}^{+\infty} \frac{\varepsilon(\Omega)}{\Omega - \omega} d\Omega = \varepsilon_1(\omega) + i\varepsilon_2(\omega) \tag{2.14}$$

where P is the main part of the integral. As we saw in condition (2) this integral equals to zero when taken over an infinite semi- circle in the upper region of the complex plane. Therefore by equating the real parts in equation (2.14) we find

$$\varepsilon_1(\omega) = \frac{1}{i\pi} P \int_{-\infty}^{+\infty} \frac{\varepsilon_2(\Omega)}{\Omega - \omega} = \frac{1}{i\pi} P \left[\int_{0}^{+\infty} \frac{\varepsilon_2(\Omega)}{\Omega - \omega} + \int_{-\infty}^{0} \frac{\varepsilon_2(\Omega)}{\lambda - \omega} d\lambda \right] \tag{2.15}$$

Replacing λ by $-\Omega$ and using the fact that $\varepsilon_2(-\Omega) = -\varepsilon_2(\omega)$ we arrive at

$$\varepsilon_1(\omega) = \frac{2}{\pi} P \int_{0}^{+\infty} \frac{\Omega \varepsilon_2(\Omega)}{\Omega^2 - \omega^2} d\Omega \tag{2.16}$$

19

Therefore by knowing the imaginary part for all frequencies, the real part of the dielectric function can be evaluated. Equating the imaginary parts in equation (2.14) and using the fact that the real part is an even function, an expression for the imaginary part of the response function can be found

$$\varepsilon_2(\omega) = -\frac{2\omega}{\pi} P \int_0^{+\infty} \frac{\varepsilon_1(\Omega)}{\Omega^2 - \omega^2} d\Omega \tag{2.17}$$

In order to apply the Kramers– Kronig relations to the reflectivity, we take the logarithm of the Fresnel coefficient of reflectivity

$$\ln r(\omega) = \ln R(\omega)^{1/2} + i\theta(\omega) \tag{2.18}$$

From FTIR reflectivity measurements $R(\omega)$ will be determined for a certain range of frequencies. Consequently the phase $\theta(\omega)$ can be evaluated using the Kramers–Kronig relations

$$\theta(\omega) = -\frac{\omega}{\pi} P \int_0^{+\infty} \frac{\ln R(\omega)}{\Omega^2 - \omega^2} d\Omega \tag{2.19}$$

Integrating equation (2.19) by parts we express the phase in the following way

$$\theta(\omega) = -\frac{1}{2\pi} P \int_0^{+\infty} \ln \left| \frac{\Omega + \omega}{\Omega - \omega} \right| \frac{d \ln R(\omega)}{d\Omega} d\Omega \tag{2.20}$$

Once the amplitude $\rho(\omega)$ and the phase $\theta(\omega)$ are known, we can go back to equations (2.11) and (2.12) to evaluate the real and imaginary parts of the complex dielectric function. The Kramers– Kronig relations require an integration of the reflectivity spectrum from zero to infinity. However, the experimental measurement of the reflectivity is always within a finite range of frequencies. This

20

appears to be a source of error when evaluating the complex dielectric function; however the IR spectrum has been measured for a wide range such that the error is minimal. The resulting dielectric function is calculated and discussed in the following section.

2.2.3   Experimental Results

The AlN polycrystalline sample investigated in this work was grown by sublimation of an AlN charge placed in the hot zone of a tungsten crucible and subsequent condensation of vapor species in a cooler region. Secondary Ion Mass spectroscopy (SIMS) measurements indicated that oxygen is the only significant impurity in the sample and a chemical analysis indicated that oxygen is presented in the sample investigated in a concentration of about 4%. High-quality surface for FT-IR measurements was prepared by chemical polishing to remove the oxide films immediately prior to the measurements.

The FT-IR reflectivity measurements were performed in vacuum in the $30 - 3000\,cm^{-1}$ frequency range. In the $30 - 350\,cm^{-1}$ frequency range, a $6\mu m/\text{Ge}$ beam splitter and a bolometer were used, while in the $350 - 3000\,cm^{-1}$, a KBr beam splitter and a DTGS detector were used. The resolution was less than $1\,cm^{-1}$. The used light was unpolarized and at near normal incidence. A microcryostat was used to vary the sample temperature from 10 °K to the room temperature.

2.3   Surface Phonon Polaritons

The large enhancement in the heat transfer in the near-field regime, as briefly mentioned in the introduction, generally originates from the coupling of the sur-

face polaritons along with the associated photon tunneling. By definition, surface polaritons are the quanta of surface-charge-density oscillations. In a classical picture, surface polaritons are particular solutions of Maxwell's equations (surface modes) that appear for certain boundary conditions. In metals and doped semiconductors, an electromagnetic field is generated due to the out of phase longitudinal oscillations of free electrons relative to the positive ion cores creates dipoles. The near-field component of the spectrum emitted is called a *surface plasmon-polariton (SPP)*. Similarly, the out of phase oscillations of transverse optical phonons in polar crystals generates an electromagnetic field, and its near-field component is called a *surface phonon-polariton (SPhP)*. *AlN* supports surface phonon polaritons in specific regions of the spectrum which would vary upon the defect state change. Harnessing the defect state change in the optical properties of oxygen contaminated *AlN* for NFRHT modulation relies on predicting the regions of existence of surface polaritons for the geometries under study and evaluating the impact of the defect state change on surface polaritons. In this section we derive the surface phonon polariton existence and resonance conditions for the semi-infinite plate and the two sphere geometries. Then, we investigate the impact of the detected defect state change in *AlN* on surface phonon polaritons for both geometries.

2.3.1   Surface Polaritons for the Semi-infinite plate

We consider the system in Figure 2.3 with: medium 1, of dielectric constant ε_{r_1} and magnetic constant μ_{r_1}, filling the lower half-space $z < 0$ and medium 2, of dielectric constant ε_{r_2}, and magnetic constant μ_{r_2}, filling the upper half-space $z > 0$. In this dissertation, we use the index r to denote the relative permittivities (dielectric constant) and permeabilities (magnetic constant). The two media are
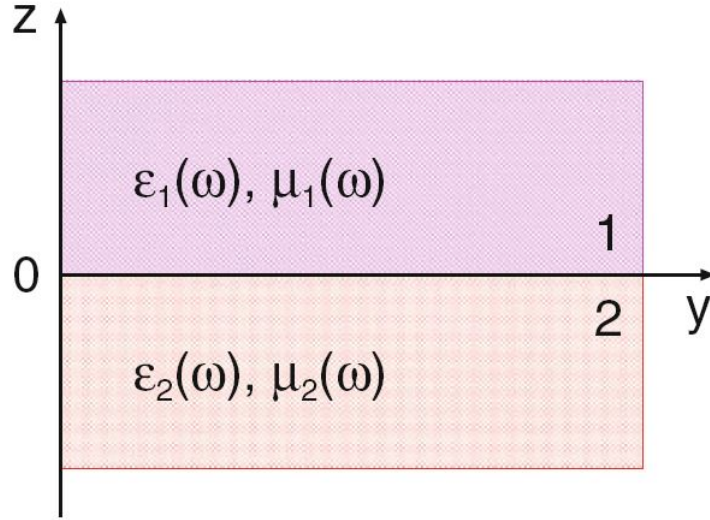
Figure 2.3: *A plane interface separating medium 1 (dielectric constant ε_{r_1}, magnetic constant μ_{r_1}) and medium 2 (dielectric constant ε_{r_2}, magnetic constant μ_{r_2})*

assumed to be local and dispersive so that their complex dielectric and magnetic constants only depend on ω.

A surface wave is a particular solution of Maxwell's equations propagating along the interface and decreasing exponentially in the perpendicular directions. A point in space is denoted as $\vec{R} = x\hat{x} + y\hat{y} + z\hat{z} = \vec{r} + z\hat{z}$, where $\vec{r} = x\hat{x} + y\hat{y}$. Similarly, a wave vector $k = (k_x, k_y, k_z) = (\vec{q}, k_z)$ where $\vec{q}$ is the component parallel to the interface and k_z is the component in the z direction. The plane wave solution decaying on the surface satisfies:

$$\vec{E}_1(\vec{R}, z) = \begin{bmatrix} E_{x,1} \\ E_{y,1} \\ E_{z,1} \end{bmatrix} exp[i(\vec{q} \cdot \vec{r} + k_{z1}z)] \tag{2.21}$$

$$\vec{E}_2(\vec{R}, z) = \begin{bmatrix} E_{x,1} \\ E_{y,1} \\ E_{z,1} \end{bmatrix} exp[i(\vec{q} \cdot \vec{r} - k_{z2}z)] \qquad (2.22)$$

$$k_{z_1} = \sqrt{\varepsilon_{r_1}\mu_{r_1}(\omega/c)^2 - q^2} \quad \Im(k_{z_1}) > 0 \qquad (2.23)$$

$$k_{z_2} = \sqrt{\varepsilon_{r_2}\mu_{r_2}(\omega/c)^2 - q^2} \quad \Im(k_{z_2}) > 0 \qquad (2.24)$$

Satisfying boundary conditions, we obtain:

$$k_{z_1}\mu_{r_2} + k_{z_2}\mu_{r_1} = 0 \quad s - polarization \qquad (2.25)$$

$$k_{z_1}\varepsilon_{r_2} + k_{z_2}\varepsilon_{r_1} = 0 \quad p - polarization \qquad (2.26)$$

Using (2.25) and (2.27) in (2.23) and (2.24) the following dispersion relation can be found for the p-polarization for non magnetic materials [27]:

$$q = \frac{\omega}{c}\sqrt{\frac{\varepsilon_1(\omega)\varepsilon_2(\omega)}{\varepsilon_2(\omega) + \varepsilon_1(\omega)}} \qquad (2.27)$$

$$k_{z_1} = \frac{\omega}{c}\sqrt{\frac{-\varepsilon_1^2(\omega)}{\varepsilon_0\left(\varepsilon_2(\omega) + \varepsilon_1(\omega)\right)}} \qquad (2.28)$$

$$k_{z_2} = \frac{\omega}{c}\sqrt{\frac{-\varepsilon_2^2(\omega)}{\varepsilon_0\left(\varepsilon_2(\omega) + \varepsilon_1(\omega)\right)}} \qquad (2.29)$$

For the case of complex ε_2 and positive real ε_1 ($\varepsilon_{vac} = 1$), $\Re(k_{z1})$ and $\Re(k_{z2})$ are positive, indicating decaying fields away from the interface, and thus surface modes, when [28, 27]:

$$|\Im(\varepsilon_{r_2})| < |\Re(\varepsilon_{r_2})| \quad and \quad \Re(\varepsilon_{r_2}) < 0 \qquad (2.30)$$

When these conditions are satisfied, surface polaritons can exist. In Figures 2.4 and 2.5, we highlight the $SPhPs$ region of existence for the parallel plates geometry for both AlN defect states of interest: H-state and L-state corresponding to the states above and below 90K respectively. However, as highlighted in section 2.1, the piezoelectric nature of AlN allows the control of the expansion and compression of the AlN unit cell, and thus imitating the effect of temperature in the oxygen-related defect complex formation, using an electric field while keeping the temperature of the material around any fixed temperature. Accordingly, oxygen defect state transition in AlN can be controlled without changing the sample temperature transitioning between two distinct states (H-state and L-state).

2.3.2   Surface Polaritons for the Spherical geometry

Now, we consider a metallic or a semiconducting sphere with radius a embedded in an infinite host medium. Region II corresponds to $0 < r < a$ (sphere), while Region I corresponds to the range $r > a$ (host medium). We use the following wave numbers in order to describe wave propagation in regions I and II:

$$k^I(\omega) = \frac{\omega}{c}\sqrt{\varepsilon_{r_1}} \tag{2.31}$$

$$k^{II}(\omega) = \frac{\omega}{c}\sqrt{\varepsilon_{r_2}} \tag{2.32}$$

The S matrix of the sphere contains all the information about the interaction of the electromagnetic field with the sphere. Applying the continuity conditions for the electric and magnetic fields at the interface between the regions, we obtain the elements of the electric part (TM) of the S matrix as:

$$S_l^E(\omega) = 1 - 2a_l^E(\omega) \tag{2.33}$$

25
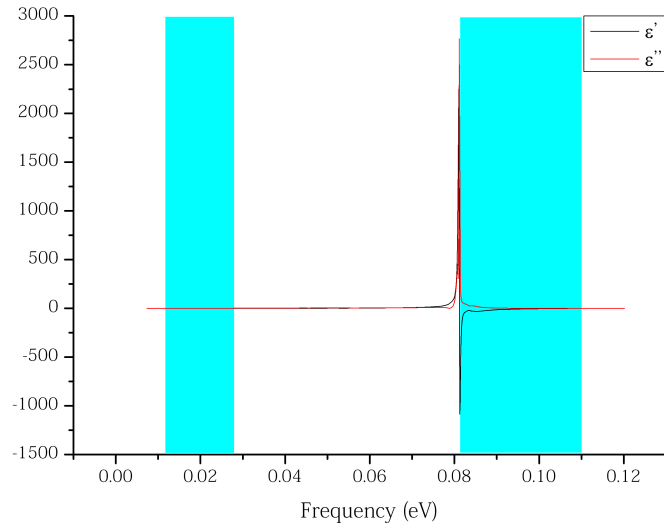
Figure 2.4: *Real (ε') and Imaginary (ε'') parts of the dielectric function of AlN in the L-state*

Figure 2.5: *Real (ε') and Imaginary (ε'') parts of the dielectric function of AlN in the H-state*

26
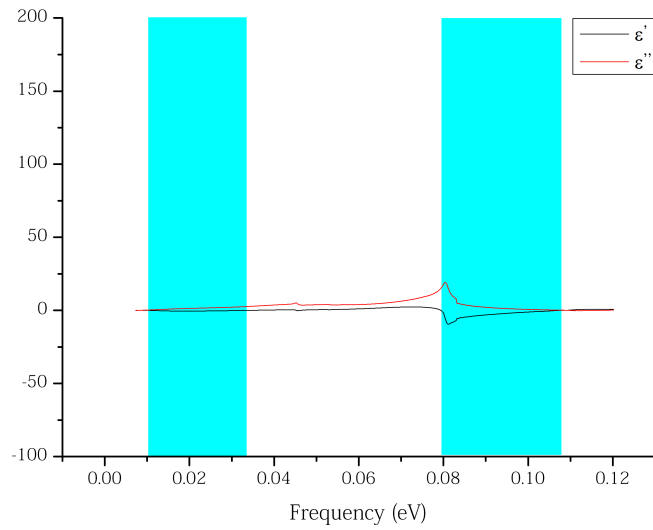
with

$$a_l^E(\omega) = \frac{C_l^E(\omega)}{D_l^E(\omega)} \tag{2.34}$$

where $C_l^E(\omega)$ and $D_l^E(\omega)$ are expressed as

$$C_l^E(\omega) = k^{II}(\omega)\psi_l[k^{II}(\omega)a]\psi_l'[k^I(\omega)a] - k^I(\omega)\psi_l[k^I(\omega)a]\psi_l'[k^{II}(\omega)a] \tag{2.35}$$

$$D_l^E(\omega) = k^{II}(\omega)\psi_l[k^{II}(\omega)a]\zeta_l^{(1)'}[k^I(\omega)a] - k^I(\omega)\zeta_l^{(1)}[k^I(\omega)a]\psi'[k^{II}(\omega)a] \tag{2.36}$$

while the elements of its magnetic part (TE) are given by:

$$S_l^M(\omega) = 1 - 2a_l^M(\omega) \tag{2.37}$$

with

$$a_l^M(\omega) = \frac{C_l^M(\omega)}{D_l^M(\omega)} \tag{2.38}$$

where $C_l^M(\omega)$ and $D_l^M(\omega)$ are expressed as

$$C_l^M(\omega) = k^{II}(\omega)\psi_l[k^I(\omega)a]\psi_l'[k^{II}(\omega)a] - k^I(\omega)\psi_l[k^{II}(\omega)a]\psi_l'[k^I(\omega)a] \tag{2.39}$$

$$D_l^M(\omega) = k^{II}(\omega)\zeta_l^{(1)}[k^I(\omega)a]\psi_l'[k^{II}(\omega)a] - k^I(\omega)\psi_l[k^{II}(\omega)a]\zeta_l^{(1)'}[k^I(\omega)a] \tag{2.40}$$

The Ricatti-Bessel functions $\psi_l(z)$ and $\zeta_l^{(1)}(z)$, are linked to the spherical Bessel functions $j_l(z)$ and $h_l^{(1)}(z)$ by $\psi_l(z) = zj_l(z)$ and $\zeta_l^{(1)}(z) = zh_l^{(1)}(z)$

The poles of the S matrix lying in the fourth quadrant of the complex ω-plane are the complex frequencies of the resonant modes ω_l. These resonances are determined by solving for the vanishing denominator of the corresponding scattering coefficient a_l thus maximizing the scattering cross-section or resonance,

27

in [29]

$$D_l^{E,M}(\omega_l) = 0 \quad for \quad l = 1, 2, 3...$$ (2.41)

We now consider these conditions in the limit of small a corresponding to small spheres. Expanding the spherical Bessel functions of order l alongside some algebra, the denominator of a_l vanishes in this limit, provided that [30]

$$\Re\{\varepsilon_r(\omega_l)\} = -\frac{l+1}{l}$$ (2.42)

2.3.3 Defect State Change and SPhP lifetimes

In Figures 2.6 and 2.7, we highlight the region where the $SPhPs$ resonance conditions apply for the spherical geometry for both AlN defect states of interest. Although the region where resonance conditions apply does not include the full region of existence of surface phonon polaritons where emission might be possible, the resonance regions help indicate the region where emission would be maximum. As demonstrated in the figures, the resonance regions shift upon the defect state transition from $[0.102eV, 0.105eV]$ to $[0.094eV, 0.1eV]$. This transition would be reflected in NFRHT spectral conductance as the maximum of transfer shifts accordingly accompanied with an increase shift in coherence upon switching defect state. The energy loss function in Fig. 2.8 as well as the imaginary part of the dielectric function (ε'') in Fig. 2.9 measure the response of the TO and LO phonons respectively. The widths of energy loss function and ε'' indicate the lifetimes of the TO and LO phonons respectively. By comparing the lifetimes of the optical phonons, one can predict an enhanced coherence upon switching from H-state to L-state determined essentially by the properties of the surface phonon polaritons.
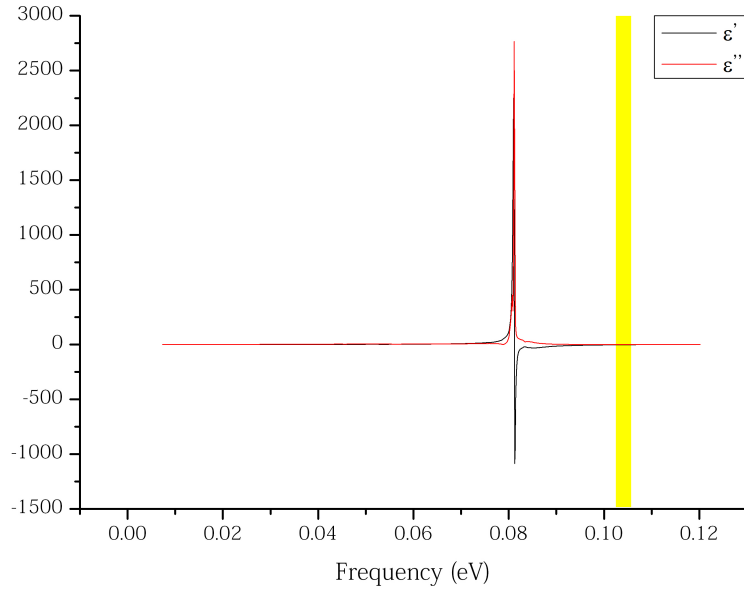
Figure 2.6: *Real (ε') and Imaginary (ε'') parts of the dielectric function of AlN in the L-state*
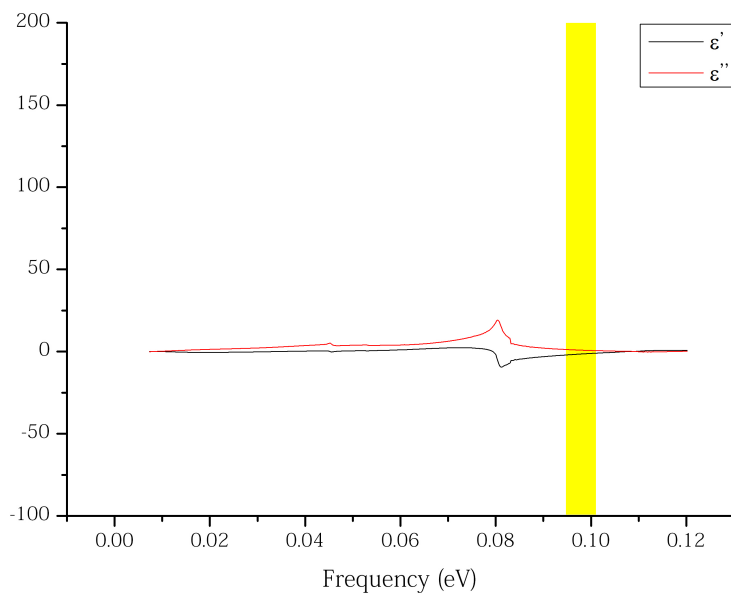
Figure 2.7: *Real (ε') and Imaginary (ε'') parts of the dielectric function of AlN in the H-state*
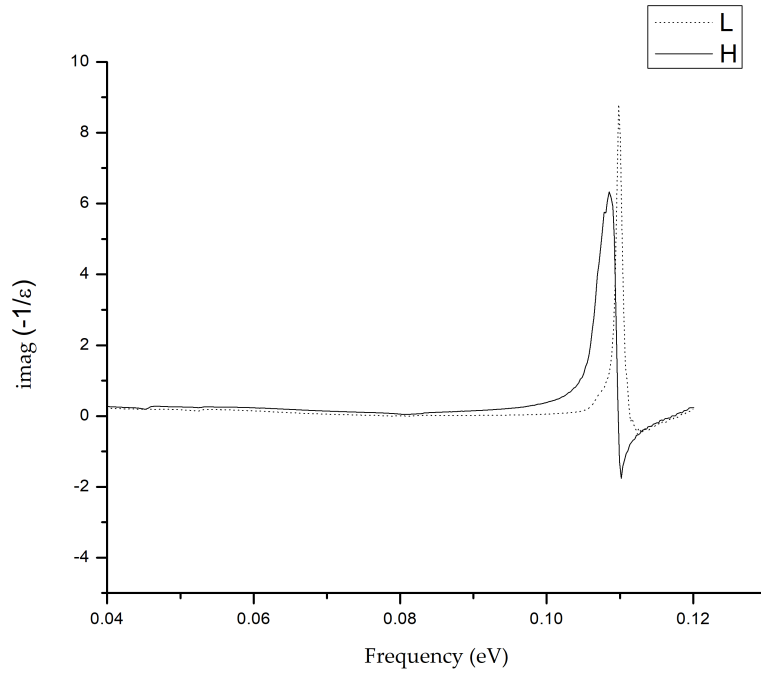
Figure 2.8: *Energy Loss Function of AlN defect states*
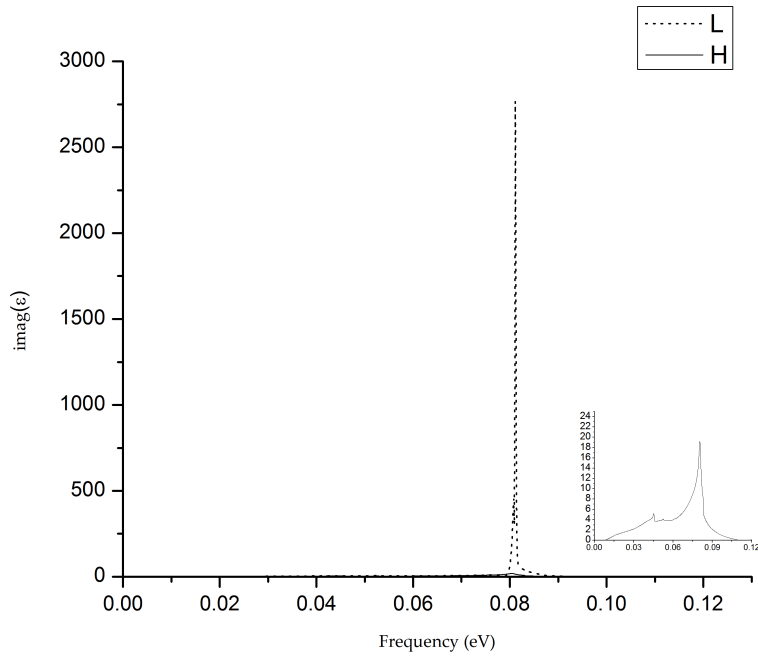
Figure 2.9: $\varepsilon_r^{''}$ *of AlN defect states*

Chapter 3

Fundamentals of Near-Field Radiative Heat Transfer

3.1 Limitations of the Classical formulation

We consider an enclosure at uniform temperature T. According to the classical formulation of thermal radiation, the electromagnetic field inside the enclosure can be described by an ensemble of photons forming standing waves with frequency ω and energy E given by $E = \hbar\omega$. The spectral mode density $D(\omega)$ or free space density of states (DOS) of photon states in the enclosure is given by

$$D(\omega) = \frac{\omega^2}{\pi^2 c^3} \tag{3.1}$$

which is derived by counting the number of states in spherical shells in k-space[31]. At thermal equilibrium the mode occupation number of the photon energy states

as governed by Bose-Einstein statistics is given by

$$n(\omega, T) = \frac{1}{e^{\hbar\omega/k_B T - 1}} \tag{3.2}$$

The spectral energy density $u^0(\omega, T)$ may be expressed as the product of the mode energy $E(\omega)$, mode occupation $n(\omega, T)$, and mode density $D(\omega)$[32]

$$u^0(\omega, T) = n(\omega, T)E(\omega)D(\omega) = \frac{\omega^2}{\pi^2 c^3} \frac{\hbar\omega}{e^{\hbar\omega/k_B T} - 1} = \Theta(\omega, T)D(\omega) \tag{3.3}$$

The radiant energy flux through an 'aperture' (area element) within a volume V, is related to the energy density and the speed of light as $q_{rad} = u^0 c/4$ [31]. By definition, a blackbody placed into that volume will absorb all of the incident radiant energy. To remain at thermal equilibrium, it must also emit that same amount of energy. Accordingly, the spectral emissive power of a blackbody $e_{b,\omega}$ is given by

$$e_{b,\omega} = \frac{\omega^2}{4\pi^2 c^2} \frac{\hbar\omega}{e^{\hbar\omega/k_B T} - 1} \tag{3.4}$$

However, unlike a blackbody which is an abstraction, real materials exhibit electron and lattice vibrational resonances resulting in spectral absorption or emission features. The spectral emissive power of a material can be characterized by three parameters: *reflection, transmission,* and *absorption* coefficients and thus exhibits resonant spectral features associated with the material's properties unlike the featureless spectrum of blackbody.

The classical approaches for the computation of net thermal transfer between black bodies are implicitly based on the ray tracing method which relies on approximate solutions to Maxwell's equations that are valid as long as the light waves propagate through and around objects whose dimensions are much greater

32

than the light's wavelength. The ray tracing approximation disregards two basic wave aspects of thermal radiation, namely: photon tunneling of evanescent waves and interference. Various attempts have been made for considering the contribution of the wave aspects of thermal radiation between objects separated by small distances beyond the thermal wavelength [33, 34, 35]. However, for conductive media the previous calculations are not appropriate because of the large imaginary part of the refractive index or the dielectric function [1]. Thus, treatment of conductive media requires the introducing the fluctuational electrodynamics formulation of thermal radiation and accounting for the evanescent surface phonon polariton modes that dominate transfer in the near-field limit. In fact, tuning the optical properties of doped Silicon between the dielectric and the conductive limit illustrates the importance of considering the fluctuational electrodynamics formulation for the origin of thermal radiation for conductive media [1, 36].

From an electromagnetic point of view, thermal radiation is related to its origin in the thermal fluctuations of charges in the medium. For an object at non-zero temperature T, thermal agitation causes a random motion of charges inside the body. These charges are mainly electrons in metals and ions in polar crystals. The random fluctuations of the charges generate a fluctuating electromagnetic field, called the thermal radiation field. Macroscopically, the field fluctuations are due to thermal fluctuations of the volume densities of the charges and current and thus can be described by *Fluctuational electrodynamics (FE)* as proposed by Rytov [2] and first simplified by Polder and Van Hove for computing thermal radiative transfer in the near-field limit [37].

Maxwell's equations provide the relation between the electromagnetic field, its source, and the material properties of the emitter. *Absorption* in Maxwell's equations is accounted for by the imaginary part of the dielectric function also

called the extinction coefficient. *Scattering* can be explained by considering the total field as the sum of the incident and scattered fields. However, thermal *emission*, which is a function of the temperature of the medium, is not considered in Maxwell's equations. The fluctuational electrodynamics formulation for thermal radiation combines the *fluctuation-dissipation theorem (FDT)*, with Maxwell's equations to fully describe thermal emission, in both the near and far-field.

3.2   Stochastic Maxwell Equations

Assuming that the time-harmonic fields have the form $e^{-i\omega t}$, Maxwell equations for non-magnetic media have the form [38, 39]:

$$\nabla \times \vec{E}(\vec{r}, \omega) = i\omega \vec{B}(\vec{r}, \omega) = i\omega\mu_0 \vec{H}(\vec{r}, \omega) \tag{3.5}$$

$$\nabla \times \vec{H}(\vec{r}, \omega) = \vec{J}(\vec{r}, \omega) - i\omega\vec{D}(\vec{r}, \omega) = \sigma\vec{E} - i\omega\hat{\varepsilon}\vec{E}(\vec{r}, \omega) = -i\omega(\hat{\varepsilon} + i\sigma/\omega)\vec{E} = -i\omega\varepsilon\vec{E} \tag{3.6}$$

$$\nabla \cdot \vec{B}(\vec{r}, \omega) = 0 \tag{3.7}$$

$$\nabla \cdot \vec{D}(\vec{r}, \omega) = \nabla \cdot \hat{\varepsilon}\vec{E}(\vec{r}, \omega) = \rho_e \tag{3.8}$$

In Ampere's law, the current density $\vec{J}$ has been combined (using Ohm's law) with the electric permittivity, leading to a complex electric permittivity $\varepsilon = \hat{\varepsilon} + i\sigma/\omega$.

The thermal fluctuations of a body around an equilibrium temperature T generate random fluctuations of current, which acts as the source for thermal radiation. Therefore, an extraneous current density term should be added in Ampere's law to account for the random thermal fluctuations of current in the

Maxwell equations [39]:

$$\nabla \times \vec{H}(\vec{r}, \omega) = -i\omega\varepsilon\vec{E} + \vec{J}^r(\vec{r}, \omega) \tag{3.9}$$

Now that the current density acts as a random source term, the Maxwell equations become stochastic in nature and are referred to as the *stochastic Maxwell equations.*

3.3 Fluctuational Electrodynamics formulation of Thermal Radiation

Adopting the method of potentials for solving Maxwell equations, the magnetic induction $\vec{B}$ can be written as

$$\vec{B}(\vec{r}, \omega) = \nabla \times \vec{A}(\vec{r}, \omega) \tag{3.10}$$

where $\vec{A}$ is referred as the magnetic vector potential. By Faraday's Law, the electric field can be written as

$$\vec{E}(\vec{r}, \omega) = i\omega\vec{A}(\vec{r}, \omega) - \nabla\phi_e(\vec{r}, \omega) \tag{3.11}$$

Using Ampere's Law (3.9),

$$\nabla \times \nabla \times \vec{A}(\vec{r}, \omega) = \mu_0\vec{J}^r(\vec{r}, \omega) + i\omega\varepsilon\mu_0\nabla\phi_e(r, \omega) + \omega^2\varepsilon\mu_0\vec{A}(r, \omega) \tag{3.12}$$

35

using vector identity $\nabla \times \nabla \times \vec{A} = \nabla(\nabla \cdot \vec{A}) - \nabla^2 \vec{A}$ and the definition of $k^2 = \omega^2 \varepsilon \mu_0$, the above equation can be simplified to

$$-\nabla(\nabla \cdot \vec{A}(\vec{r}, \omega)) + \nabla^2 \vec{A}(\vec{r}, \omega) + k^2 \vec{A}(\vec{r}, \omega) = -\mu_0 \vec{J}^r(\vec{r}, \omega) - i\omega\varepsilon\mu_0 \nabla \phi_e(\vec{r}, \omega) \quad (3.13)$$

Using the Lorenz gauge by letting $\nabla \cdot \vec{A}(\vec{r}, \omega) = i\omega\varepsilon\mu_0\phi_e(\vec{r}, \omega)$, we obtain the *vector Helmholtz equation* [39, 40]

$$(\nabla^2 + k^2)\vec{A}(\vec{r}, \omega) = -\mu_0 \vec{J}^r(\vec{r}, \omega) \quad (3.14)$$

Therefore, the magnetic vector potential can then be expressed as

$$A(\vec{r}, \omega) = \mu_0 \int_V \vec{J}^r(r, \omega) g(\vec{r}, \vec{r'}, \omega) dV' \quad (3.15)$$

where $g(\vec{r}, \vec{r'}, \omega)$ is the Green's function which is the solution of the field at $\vec{r}$ for a point source at $\vec{r'}$ described by the Dirac delta function as

$$(\nabla^2 + k^2)g(\vec{r}, \vec{r'}, \omega) = -\delta(|\vec{r} - \vec{r'}|) \quad (3.16)$$

The electric and magnetic fields are then given by using (3.15) in (3.11) and (3.10) [39, 40]

$$\vec{E}(\vec{r}, \omega) = i\omega\mu_0 \int_V dV' g(\vec{r}, \vec{r'}, \omega)[\mathbf{I} + \frac{1}{k^2}\nabla\nabla] \cdot \vec{J}^r(\vec{r'}, \omega) \quad (3.17)$$

$$\vec{H}(\vec{r}, \omega) = \nabla \times \int_V dV' g(\vec{r}, \vec{r'}, \omega)\mathbf{I} \cdot \vec{J}^r(\vec{r'}, \omega) \quad (3.18)$$

36

Where $\mathbf{I} = \hat{x}\hat{x} + \hat{y}\hat{y} + \hat{z}\hat{z}$ is the identity dyad. Furthermore, the electric and magnetic field can be written in terms of dyadic Green's function defined as [39]

$$\mathbf{G}^e(\vec{r}, \vec{r'}, \omega) = g(\vec{r}, \vec{r'}, \omega)[\mathbf{I} + \frac{1}{k^2}\nabla\nabla] \tag{3.19}$$

$$\mathbf{G}^m(\vec{r}, \vec{r'}, \omega) = \nabla \times (g(\vec{r}, \vec{r'}, \omega)\mathbf{I}) \tag{3.20}$$

The electric and magnetic dyadic Green's functions are related by the following relation:

$$\mathbf{G}^m(\vec{r}, \vec{r'}, \omega) = \nabla \times \mathbf{G}^e \tag{3.21}$$

The electric and magnetic fields can be written as

$$\vec{E}(\vec{r}, \omega) = i\omega\mu_0 \int_V dV' \mathbf{G}^e \cdot \vec{J^r}(\vec{r'}, \omega) \tag{3.22}$$

Example of calculating ith component of $E(r, \omega)$:

$$\begin{aligned} E_i &= i\omega\mu_0 \int_V dV' (G^e_{ix}\hat{x} + G^e_{iy}\hat{y} + G^e_{iz}\hat{z}) \cdot (J^r_x\hat{x} + J^r_y\hat{y} + J^r_z\hat{z}) \\ &= i\omega\mu_0 \int_V dV' (G^e_{ix}J^r_x + G^e_{iy}J^r_y + G^e_{iz}J^r_z\hat{z}) \\ &= i\omega\mu_0 \int_V dV' G^e_{in}J^r_n \end{aligned} \tag{3.23}$$

where the subscript n involves the summation over the three orthogonal components. Similarly, for the magnetic field can be written as

$$\vec{H}(\vec{r}, \omega) = i\omega\mu_0 \int_V dV' \mathbf{G}^m \cdot \vec{J^r}(\vec{r'}, \omega) \tag{3.24}$$

with an *ith* component

$$H_i = i\omega\mu_0 \int_V dV'(G_{ix}^m \hat{x} + G_{iy}^m \hat{y} + G_{iz}^m \hat{z}) \cdot (J_x^r \hat{x} + J_y^r \hat{y} + J_z^r \hat{z})$$
$$= i\omega\mu_0 \int_V dV'(G_{ix}^m J_x^r + G_{iy}^m J_y^r + G_{iz}^m J_z^r \hat{z}) \qquad (3.25)$$
$$= i\omega\mu_0 \int_V dV' G_{in}^m J_n^r$$

The time-averaged Poynting vector, which can be measured, is expressed as [38, 39]

$$\langle S(\vec{r}, \omega) \rangle$$
$$= 4 \times \frac{1}{2}\Re\{\vec{E}(\vec{r}, \omega) \times \vec{H}^*(\vec{r}, \omega)\}$$
$$= 2 \times \Re\left\{\hat{x}(E_y H_z^* - E_z H_y^*) + \hat{y}(E_z H_x^* - E_x H_z^*) + \hat{z}(E_x H_y^* - E_y H_x^*)\right\}$$
$$= 2\Re\left\{i\omega\mu_0 \int_V dV' \int_V dV'' \begin{bmatrix} \hat{x}(G_{yn}^e G_{zj}^{m*} - G_{zn}^e G_{yj}^{m*}) \\ +\hat{y}(G_{zn}^e G_{xj}^{m*} - G_{xn}^e G_{zj}^{m*}) \\ +\hat{z}(G_{xn}^e G_{yj}^{m*} - G_{yn}^e G_{xj}^{m*}) \end{bmatrix} \langle \vec{J}_n^r(\vec{r'}, \omega)\vec{J}_j^{r*}(\vec{r''}, \omega) \rangle\right\}$$

$$(3.26)$$

The factor of 4 is connected with fact that: the integration is assumed only over positive values of ω that are considered in the Fourier decomposition of the time-dependent fields into frequency-dependent quantities thus a factor of 2 is included [40]; at the same time, the transformation of integration over infinite interval to semi-infinite interval gives an additional factor of 2 [39].

Since the randomness of the current density is due to the thermal fluctuations, the spectral density of the fluctuating current $\langle \vec{J}_n^r(\vec{r'}, \omega)\vec{J}_j^{r*}(\vec{r''}, \omega) \rangle$ which acts as a stochastic source term of thermal radiation should be related to the local temperature of the emitter. The *fluctuation-dissipation theorem (FDT)* bridges

38

the spectral density of the fluctuating current sources with the local temperature of the emitter. Although the random currents have zero mean, the observables of interest such as the Poynting vector and the spectral energy density are quadratic in the field components. The average value of any quadratic observable can be calculated starting from the correlation of the electric field $\langle E_i(\vec{r}, t) E_j(\vec{r}', t') \rangle$ whose Fourier transform does not vanish [41].

The general FDT is based on the following assumptions [39]:

1. the body is in thermodynamic equilibrium at an equilibrium temperature T around which there are fluctuations

2. isotropic medium

3. non-magnetic medium defined by a frequency-dependent dielectric constant $\varepsilon_r(\omega)$ investigated in Chapter 2.

4. the dielectric constant is local in space (i.e., the polarization at a given point in a medium is directly proportional to the electric field at that point, and does not directly depends on the fields from other points), and consequently the fluctuations are uncorrelated between neighboring volume elements

Using FDT, the spectral density of the current fluctuations can be determined as [42]:

$$\langle J_n^r(\vec{r'}, \omega) J_j^{r*}(\vec{r''}, \omega) \rangle = \frac{\omega \varepsilon_0}{\pi} \Im\{\varepsilon_r(\omega)\} \Theta(\omega, T) \delta_{nj} \delta(\vec{r'} - \vec{r''}) \qquad (3.27)$$

where $\Theta(\omega, T) = \frac{\hbar\omega}{e^{\hbar\omega/k_B T} - 1}$ is the mean energy of a Planck oscillator in thermal equilibrium at an angular frequency ω and at temperature T. The locality of the dielectric constant shows up in the spectral density through the Dirac function while the isotropy of the medium is expressed by the Kronecker delta. Furthermore, the imaginary of the dielectric constant, or the extinction coefficient, shows
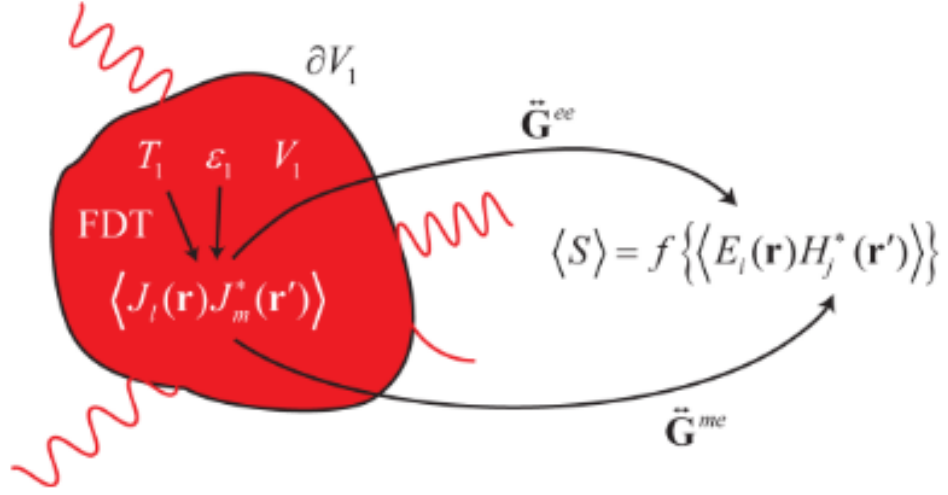
39

Figure 3.1: *Schematic of the Poynting vector of the electromagnetic fields E and H generated by the random currents J in the emitter*

up as it generally describes the absorption/dissipation of thermal radiation inside an irradiated body.

The spectral density of the fluctuating currents can then be substituted in the Poynting vector and the energy density to obtain [43, 44]:

$$
\langle S(r,\omega) \rangle
$$

$$
= \frac{2\varepsilon_0\mu_0\omega^2}{\pi}\Re\left\{ i\int_V dV' \int_V dV''
\begin{bmatrix}
\hat{x}(G^e_{yn}G^{m*}_{zj} - G^e_{zn}G^{m*}_{yj}) \\
+\hat{y}(G^e_{zn}G^{m*}_{xj} - G^e_{xn}G^{m*}_{zj}) \\
+\hat{z}(G^e_{xn}G^{m*}_{yj} - G^e_{yn}G^{m*}_{xj})
\end{bmatrix}
\Im\{\varepsilon_r(\omega)\}\Theta(\omega,T)\delta_{nj}\delta(\vec{r}' - \vec{r}'') \right\}
$$

$$
= \frac{2\varepsilon_0\mu_0\omega^2}{\pi}\Theta(\omega,T)\Re\left\{ i\Im\{\varepsilon_r(\omega)\}\int_V dV' G^e_{\alpha n}(\vec{r},\vec{r}',\omega)G^{m*}_{\beta n}(\vec{r},\vec{r}',\omega) \right\} \quad (3.28)
$$

The subscripts α and β represent the state of polarization of the fields observed at $\vec{r}$, while n represents the state of polarization of the source at $\vec{r}'$. The set of indices αn implies that a summation is performed over all components (i.e. $xx + xy +$

$\cdots + zz)$. The Poynting vector as expressed in (3.28) form a general relation for calculating the radiative heat flux accounting for the near-field effects of thermal radiation. For a specific geometry and boundary conditions, the components of the dyadic Green's functions are to be determined.

In the case of thermal *equilibrium* situations, the spectral density of the current is used to calculate quantities such as the energy density and the Poynting vector. However, in *non-equilibrium* situation such as the study of heat transfer between materials held at different temperatures as studied in the following section, these expressions are no longer valid. It is however still possible to use the fluctuation-dissipation theorem for the currents by assuming local thermal equilibrium and thus render possible the derivation of the fluxes for non-equilibrium situations [41].

3.4 Radiative Heat Transfer between two Parallel Plates

We consider the near-field radiative heat transfer between for the two semi-infinite plates configuration. The plates each at thermal equilibrium at T_1 and T_2 respectively are separated by a vacuum gap of width d. For computing the near-field radiative transfer between the plates, the green function for the two plates configuration is needed. Starting with the configuration in Figure 3.2, we consider a monochromatic electromagnetic wave originated from medium 1 to 2, $e^{i\vec{k_j}\cdot\vec{x}-i\omega t}$. The complex wave vectors in media 1 and 2 are k_1 and k_2, respectively, with $k_1^2 = \varepsilon_{r_1}k_0^2$ and $k_2^2 = \varepsilon_{r_2}k_0^2$ where $k_0 = \omega/c$ is the magnitude of the wave vector in vacuum. β refers to the parallel component to the interface of the wave vector while γ_j refers to the r-component of the wave vectors $\vec{k_j} = \beta\hat{r} + \gamma_j\hat{z}$ with

41

(a) Closely spaced parallel plates
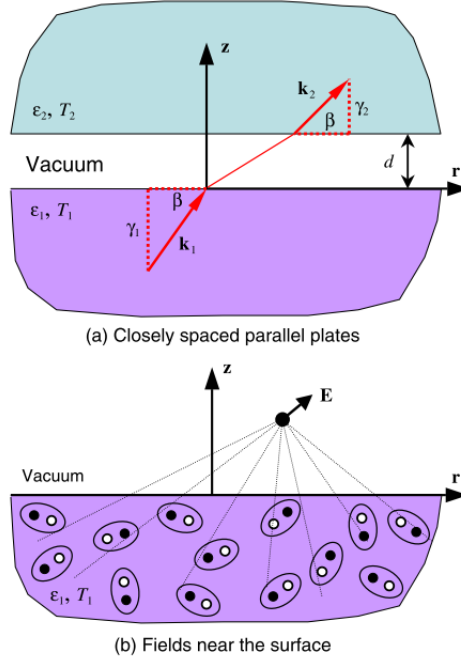

(b) Fields near the surface

Figure 3.2: *Schematic of the two closely spaced parallel plates configuration*

$j = 0, 1,$ *or* 2 referring to the medium. The Green function corresponding to the two parallel plates configuration is given by [45, 46]

$$\mathbf{G}(\vec{x}, \vec{x'}, \omega) = \frac{i}{4\pi} \int_0^\infty \frac{\beta d\beta}{\gamma_1} (\hat{s} t_{12}^s \hat{s} + \hat{p}_2 t_{12}^p \hat{p}_1) e^{i\gamma_2 z - i\gamma_1 z'} e^{i\beta\hat{r}\cdot(\vec{r}-\vec{r'})} \qquad (3.29)$$

where t_{12}^s and t_{12}^p denoting the transmission coefficients from medium 1 to medium 2, taken to be the Fresnel transmission coefficients for vacuum separated plates, for s and p polarizations, respectively, with the unit vectors defined as $\hat{s} = \hat{r} \times \hat{z}$, $\hat{p}_1 = (\beta\hat{z} - \gamma_1\hat{r})/k_1$ and $\hat{p}_2 = (\beta\hat{z} - \gamma_2\hat{r})/k_2$.

With the assistance of the dyadic Green's function, the net spectral flux can be predicted by subtracting the fluxes using Eq 3.28 as [46]

$$q(\omega) = \frac{1}{\pi^2} [\Theta(\omega, T_1) - \Theta(\omega, T_2)] \int_0^\infty s_\beta(\omega, \beta) d\beta \qquad (3.30)$$

42

$$s_\beta(\omega, \beta) = \begin{cases} s_{prop}(\omega,\beta) = \frac{\beta(1-\rho_{01}^s)(1-\rho_{02}^s)}{4\left|1-r_{01}^s r_{02}^s e^{i2\gamma_0 d}\right|^2} + \frac{\beta(1-\rho_{01}^p)(1-\rho_{02}^p)}{4\left|1-r_{01}^p r_{02}^p e^{i2\gamma_0 d}\right|^2} & \beta < \omega/c \\ s_{evan}(\omega,\beta) = \frac{\Im(r_{01}^s)\Im(r_{02}^s)\beta e^{-2\Im(\gamma_0)d}}{\left|1-r_{01}^s r_{02}^s e^{-2\Im(\gamma_0)d}\right|^2} + \frac{\Im(r_{01}^p)\Im(r_{02}^p)\beta e^{-2\Im(\gamma_0)d}}{\left|1-r_{01}^p r_{02}^p e^{-2\Im(\gamma_0)d}\right|^2} & \beta > \omega/c \end{cases} \tag{3.31}$$

where the coefficients r_{0j}^s and r_{0j}^p are the Fresnel reflection coefficients, for s and p polarization respectively, at the interface between vacuum and medium j (1 or 2) and $\rho_{01} = |r_{01}|^2$

$$r_{0j}^s = \frac{\gamma_0 - \gamma_j}{\gamma_0 + \gamma_j} \tag{3.32}$$

$$r_{0j}^p = \frac{\varepsilon_{j_r}\gamma_0 - \gamma_j}{\varepsilon_{j_r}\gamma_0 + \gamma_j} \tag{3.33}$$

The spectral heat transfer coefficient $h(\omega; T)$ for this geometry is thus given by:

$$h(\omega; T) = \lim_{T_1 \to T_2} \frac{q(\omega)}{|T_1 - T_2|} = k_B \left(\frac{\hbar\omega}{k_B T}\right)^2 \frac{e^{\hbar\omega/k_B T}}{(e^{\hbar\omega/k_B T} - 1)^2} \frac{1}{\pi^2} \int_0^\infty s_\beta(\omega, \beta)d\beta \tag{3.34}$$

3.5 Tuning of Near Field Radiative Transfer between AlN Parallel Plates

In Fig. 3.3, we plot the spectral heat transfer coefficient spanning gaps of several orders of magnitude in the near-field limit $d = 1, 10, 100, 1000\,nm$ for both defect states of AlN at room temperature (300K) where in each both plates are in the same defect state. The slope for the net heat transfer coefficient logarithmic plot along with the spectral heat transfer coefficient plots for each gap demonstrate as expected the d^{-2} dependence for net transfer as a function of gap separation for small gaps. The spectral heat transfer coefficient for the L-state, as predicted in Chapter 2, shows a more coherent signal than the H-
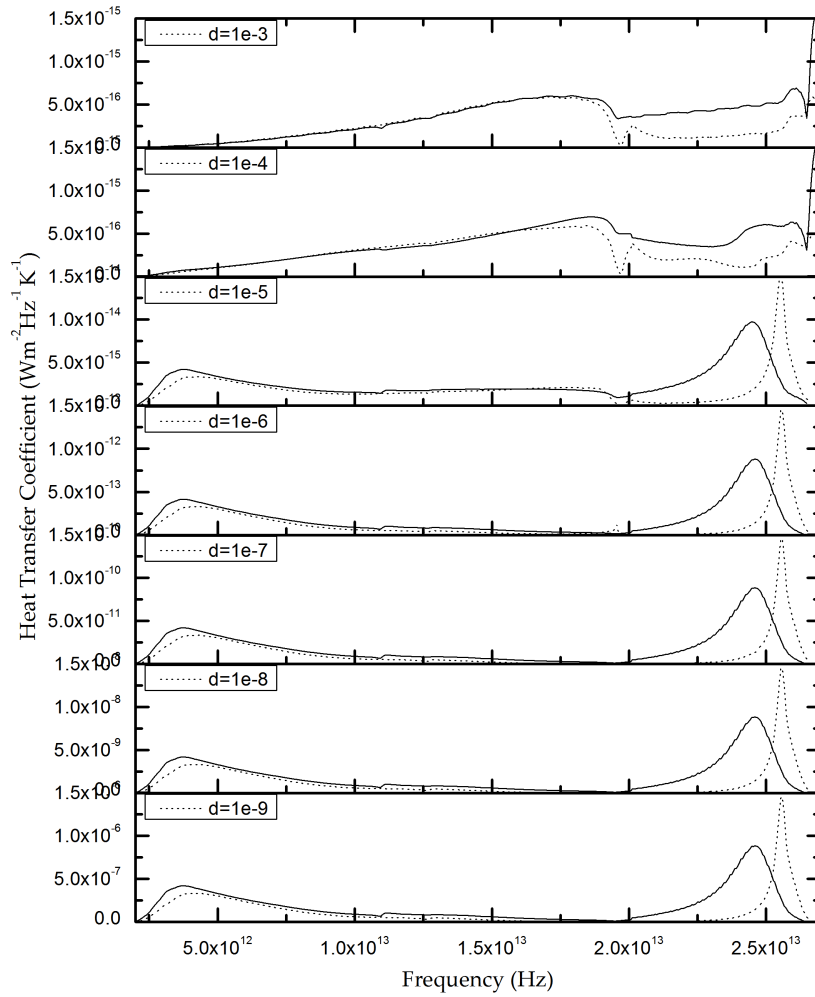
Figure 3.3: *Heat Transfer Coefficient of Near-field Radiation for AlN defect at various gap separations states*
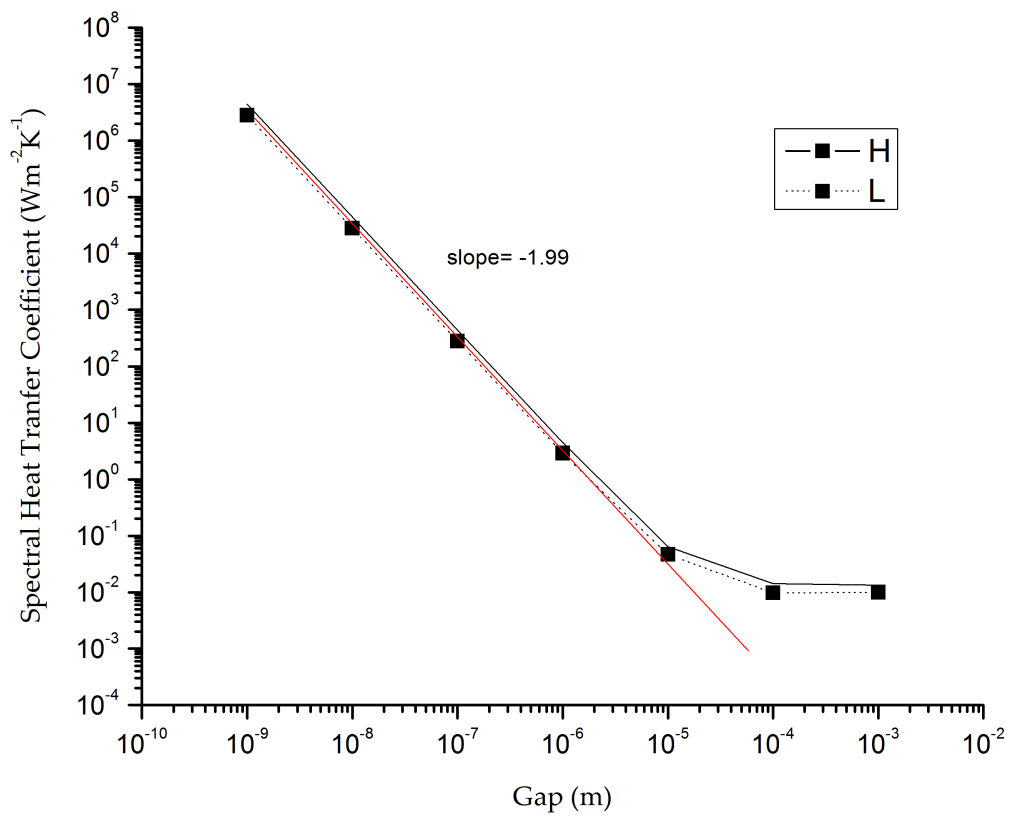
Figure 3.4: *Variation of Heat Transfer Coefficient with Gap for AlN defect states*

state; this drop is also accompanied with a drop in magnitude allowing for an appreciable modulation of thermal transfer. The NFRHT is modulated by 36% for gaps of different orders of magnitude in the near-field limit. The coherence as quantified by the FWHM of the spectral heat transfer coefficient corresponding to the frequency range corresponding to the reststrahlen band is increased by a factor of 3.7 for the L-state for the different gaps investigated.

Chapter 4

Near-field Radiative Heat Transfer between two spheres

The Narayanaswamy and Chen model [22] for NFRHT between two spheres is valid for arbitrary sphere sizes and vacuum gaps and is not limited by the point dipole approximation valid for very small spheres nor by the proximity force theorem valid for large spheres separated by a very small gap. Based on this model, the near-field radiative heat transfer between two spheres is investigated under the fluctuational electrodynamics framework using the dyadic Green's functions (DGF) of the vector Helmholtz equation in spherical coordinates. We develop a MATLAB code for computing the NFRHT between two spheres based on Narayanaswamy and Chen model and predicting NFRHT modulation for oxygen contaminated AlN spheres.
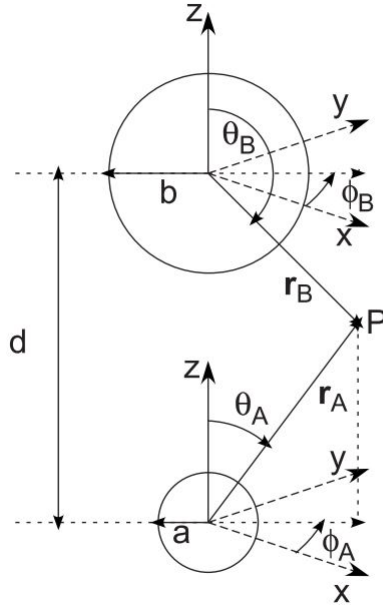
Figure 4.1: *The two sphere configuration*

4.1 Fluctuational Electrodynamics Formulation for the Two Spheres Problem

4.1.1 The Two Sphere Problem Configuration

We consider two non-overlapping spheres of radii a and b separated by a distance d as in Figure (4.1). At the center of each sphere is a spherical coordinate system oriented such that the two spheres lie along the common z axis and the ϕ coordinate is the same in both systems. Region A(B) refers to the interior of spheres A(B) while region C refers to the exterior of both spheres (the vacuum gap).

4.1.2 The Dyadic Green Functions

Defining $\vec{r_1}$ and $\vec{r_2}$ to be the points on either side of the boundary and $\hat{n}$ is a unit normal to the boundary surface at $\vec{r_1}$ and $\vec{r_2}$, the DGF satisfies the following boundary conditions to ensure the continuity of tangential electric and magnetic fields [22]:

$$\vec{n} \times \mathbf{G}^e(\vec{r_1}, \vec{r'}) = \hat{n} \times \mathbf{G}^e(\vec{r_2}, \vec{r'}) \tag{4.1}$$

$$\vec{n} \times \nabla \times \mathbf{G}^e(\vec{r_1}, \vec{r'}) = \hat{n} \times \nabla \times \mathbf{G}^e(\vec{r_2}, \vec{r'}) \tag{4.2}$$

Unlike typical electromagnetic waves scattering problem, for calculating the power emitted by a sphere, the DGF has to be determined when the source point is in the interior of the sphere. The DGF is expanded in terms of vector spherical waves (VSW), which are solutions of

$$\nabla \times \nabla \times \vec{P}(\vec{r}) - k^2 \vec{P}(\vec{r}) = 0 \tag{4.3}$$

Dropping the "incoming" vector solutions, the vector spherical waves needed include the "radiating" and "regular" wave solutions [47]:

$$\vec{M}_{lm}^{(p)}(k\vec{r}) = z_l^{(p)}(kr)\vec{V}_{lm}^{(2)}(\theta, \phi) \tag{4.4}$$

$$\vec{N}_{lm}^{(p)}(k\vec{r}) = \zeta_l^{(p)}(kr)\vec{V}_{lm}^{(3)}(\theta, \phi) + \frac{z_l^{(p)}(kr)}{kr}\sqrt{l(l+1)}\vec{V}_{lm}^{(1)}(\theta, \phi) \tag{4.5}$$

$M_{lm}^{(p)}$ and $N_{lm}^{(p)}$ are VSW of order (l, m), where l can take integer values from 0 to ∞, and for each l, $|m| \leq l$. The superscript p refers to the radial behavior of the waves. For $p = 1$, the M and N waves are regular waves and remain finite at the origin and $z_l^{(1)}(kr)$ is the spherical Bessel function of order l. For $p = 3$,

49

the M and N waves are outgoing spherical waves that are singular at the origin and $z_l^{(3)}(kr)$ is the spherical Hankel function of the first kind of order l. The radial functions are defined as $\zeta_l^{(p)}(x) = (\frac{1}{x}\frac{d}{dx}xz_l^{(p)}(kr))$. The vectors $\vec{V}_{lm}^{(1)}(\theta,\phi)$, $\vec{V}_{lm}^{(2)}(\theta,\phi)$, and $\vec{V}_{lm}^{(3)}(\theta,\phi)$ are vector spherical harmonics of order (l,m), expressed as:

$$\vec{V}_{lm}^{(2)}(\theta,\phi) = \hat{r}Y_{lm} \tag{4.6}$$

$$\vec{V}_{lm}^{(1)}(\theta,\phi) = \frac{1}{\sqrt{l(l+1)}}\left(-\hat{\phi}\frac{\partial Y_{lm}}{\partial \theta} + \hat{\theta}\frac{im}{\sin\theta}Y_{lm}\right) \tag{4.7}$$

$$\vec{V}_{lm}^{(3)}(\theta,\phi) = \frac{1}{\sqrt{l(l+1)}}\left(\hat{\theta}\frac{\partial Y_{lm}}{\partial \theta} + \hat{\phi}\frac{im}{\sin\theta}Y_{lm}\right) \tag{4.8}$$

Any solution to Eq. 4.3 can be expressed as a linear combination of the VSWs. To satisfy the boundary conditions on the surface of each sphere, the VSWs of one coordinate system should be expressed in terms of the VSWs of the other coordinate system using the translation addition theorem for vector spherical waves. Once the Green's function satisfying boundary conditions for the two sphere configuration is determined, the Poynting vector denoting the heat flux from one sphere to another can be calculated. Finally, the net radiative heat transfer can be concluded.

The vector translation addition theorem states expressing the VSW in coordinate system B in terms of coordinates system A is expressed as [48, 22]:

$$\vec{M}_{lm}^{(p)}(k\vec{r}_b) = \sum_{\substack{\mu=-\nu \\ \nu=1}}^{\substack{\nu=\infty \\ \mu=\nu}}\left[A_{\nu\mu}^{lm}(+kd)\vec{M}_{\nu\mu}^{(p)}(kr_a) + B_{\nu\mu}^{lm}(+kd)\vec{N}_{\nu\mu}^{(p)}(kr_a)\right] \tag{4.9}$$

$$\vec{N}_{lm}^{(p)}(k\vec{r}_b) = \sum_{\substack{\mu=-\nu \\ \nu=1}}^{\substack{\nu=\infty \\ \mu=\nu}}\left[B_{\nu\mu}^{lm}(+kd)\vec{M}_{\nu\mu}^{(p)}(kr_a) + A_{\nu\mu}^{lm}(+kd)\vec{N}_{\nu\mu}^{(p)}(kr_a)\right] \tag{4.10}$$
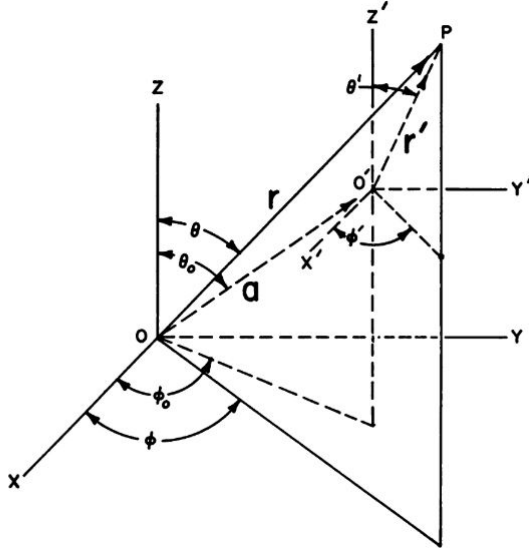
Figure 4.2: *Coordinate Translation*

The VSW in coordinate system B need to be expressed in terms of on the coordinates of system A and vice versa to satisfy boundary conditions. The coefficients $B_{\nu\mu}^{lm}$ and $A_{\nu\mu}^{lm}$ as expressed in Ref. [48] depend on the orientation of translating vector between the two systems as in Fig 4.1.2. The coefficients $B_{\nu\mu}^{lm}(-kd)$ and $A_{\nu\mu}^{lm}(-kd)$ are required and can be obtained through symmetry relations with $B_{\nu\mu}^{lm}(+kd)$ and $A_{\nu\mu}^{lm}(+kd)$. In the case of the two-sphere problem, with translation along the z axis Eq. 4.9 and Eq. 4.10 simplifies so that the coefficients are nonzero for $\mu = m$, thus the needed coefficients are $B_{\nu m}^{lm}$ and $A_{\nu m}^{lm}$.

4.1.3 Recurrence Relations

Generally, determining the coefficients of translation theory $B_{\nu\mu}^{lm}$ and $A_{\nu\mu}^{lm}$ is computationally expensive as this requires calculations of Wigner $3j$ symbols which involve calculations of large number of factorials. Recurrence relations for computing the coefficients efficiently have been proposed for improving computations [49, 50]. The coefficients $B_{\nu m}^{lm}$ and $A_{\nu m}^{lm}$ for the vector addition theorem can be
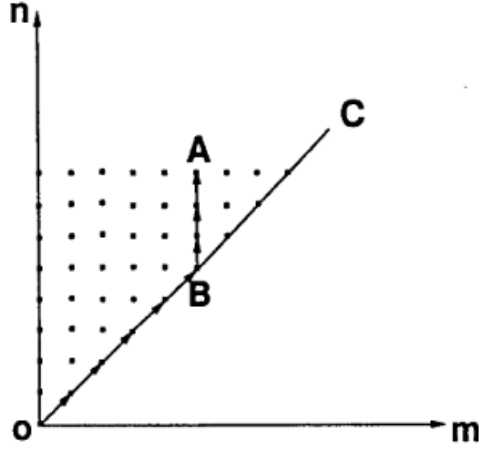
Figure 4.3: *A representation of employing recursive relations in calculating the scalar translation matrix coefficients*

related to the coefficients $\beta_{\nu\mu,nm}$ of the *scalar addition theorem* as investigated in Ref. [50]. Recurrence relations for the calculation the coefficients $\beta_{\nu\mu,nm}$ have been derived in Ref. [49]. Thus, the coefficients $B_{\nu m}^{lm}$ and $A_{\nu m}^{lm}$ can be accordingly efficiently calculated as [50]:

$$A_{\nu m}^{lm}(k_f d) = \beta_{\nu m,lm} + k_f d \frac{1}{\nu + 1} \sqrt{\frac{(\nu + m + 1)(\nu - m + 1)}{(2\nu + 1)(2\nu + 3)}} \beta_{\nu+1,m,lm}$$
$$+ k_f d \frac{1}{\nu} \sqrt{\frac{(\nu + m)(\nu - m)}{(2\nu - 1)(2\nu + 1)}} \beta_{\nu-1,m,lm} \quad (4.11)$$

$$B_{\nu m}^{lm}(k_f d) = k_f d \frac{im}{\nu(\nu + 1)} \beta_{\nu m,lm} \quad (4.12)$$

There are two recursive relations for the calculation of coefficients for the scalar addition theorem that can be used for determining the scalar translation coefficients as demonstrated schematically in Fig. 4.3 [49]:

$$a_{nm}^{+}\beta_{\nu\mu,n+1,m} = -a_{nm}^{-}\beta_{\nu\mu,n-1,m} + a_{\nu-1,\mu}^{+}\beta_{\nu-1,\mu,nm} + a_{\nu+1,\mu}^{-}\beta_{\nu+1,\mu,nm} \quad (4.13)$$

$$b_{nm}^+ \beta_{\nu\mu,n+1,m+1} = -b_{nm}^- \beta_{\nu\mu,n-1,m+1} + b_{\nu-1,\mu-1}^+ \beta_{\nu-1,\mu-1,nm} + b_{\nu+1,\mu-1}^- \beta_{\nu+1,\mu-1,nm}$$

$$(4.14)$$

The starting point for calculating any $\beta_{\nu\mu,nm}$ is the coefficient

$$\beta_{\nu0,00} = (-1)^\nu \sqrt{2\nu + 1} j_\nu(k_f d) \qquad (4.15)$$

4.1.4 Scattering Theory in the two Sphere Problem

Based on the scattering theory, the DGF for any configuration can be split into two parts: one that corresponds to a Dirac-delta source in an infinite medium $\mathbf{G}_0$ and one that takes into account the scattering $\mathbf{G}_{sc}$. The free space dyadic green function $\mathbf{G}_0$ for a sphere is expressed in Ref.[51] . In our case, the source point is confined to the interior of sphere A, therefore we are interested in the case where $r_a > r'_a$, whereas the boundary of interest is the surface of the sphere.

$$\mathbf{G}_0(\vec{r_a}, \vec{r'_a}) = \frac{\hat{r}\hat{r}}{k_a}\delta(\vec{r_a} - \vec{r'_a}) + ik_a \sum_{\substack{m=-l \\ l=1}}^{\substack{l=\infty \\ m=l}} \begin{cases} \vec{M}_{l,m}^{(1)}(k_a\vec{r_a})\vec{M}_{l,-m}^{(3)}(k_a\vec{r'_a}) + \vec{N}_{l,m}^{(1)}(k_a\vec{r_a})\vec{N}_{l,-m}^{(3)}(k_a\vec{r'_a}) & if \quad r_a < r'_a \\ \vec{M}_{l,m}^{(3)}(k_a\vec{r_a})\vec{M}_{l,-m}^{(1)}(k_a\vec{r'_a}) + \vec{N}_{l,m}^{(3)}(k_a\vec{r_a})\vec{N}_{l,-m}^{(1)}(k_a\vec{r'_a}) & if \quad r_a < r'_a \end{cases}$$

$$(4.16)$$

Inside A, the DGF is a combination of $\mathbf{G}_0$ and $\mathbf{G}_{sc}$, whereas outside A, the DGF is entirely $\mathbf{G}_{sc}$. Each term, $M_{l,m}^{(3)}(k_a\vec{r'}_a)$ or $N_{l,m}^{(3)}(k_a\vec{r'}_a)$ can be thought of as an independent vector spherical waves that produces scattered waves. As an example of the scattered field due to $M_{l,m}^{(3)}(k_a\vec{r'}_a)$ of order (l,m) in the three regions

$$\sum_{\nu=(m,1)}^{\infty} \begin{cases} ik_a[A_{\nu m}^{lM}\vec{M}_{\nu,m}^{(1)}(k_a r_a) + A_{\nu m}^{lN}\vec{N}_{\nu,m}^{(1)}(k_a r_a)] + [B_{\nu m}^{lM}\vec{M}_{\nu,m}^{(3)}(k_a r_b) + B_{\nu m}^{lN}\vec{N}_{\nu,m}^{(3)}(k_a r_b)] & in \quad A \\ ik_f[C_{\nu m}^{lM}\vec{M}_{\nu,m}^{(3)}(k_f r_a) + C_{\nu m}^{lN}\vec{N}_{\nu,m}^{(3)}(k_f r_a)] + [D_{\nu m}^{lM}\vec{M}_{\nu,m}^{(3)}(k_f r_b) + D_{\nu m}^{lN}\vec{N}_{\nu,m}^{(3)}(k_f r_b)] & in \quad C \\ ik_b[E_{\nu m}^{lM}\vec{M}_{\nu,m}^{(3)}(k_b r_a) + E_{\nu m}^{lN}\vec{N}_{\nu,m}^{(3)}(k_b r_a)] + [F_{\nu m}^{lM}\vec{M}_{\nu,m}^{(1)}(k_b r_b) + F_{\nu m}^{lN}\vec{N}_{\nu,m}^{(1)}(k_b r_b)] & in \quad B \end{cases} \quad (4.17)$$

where the symbol (m,1) refers to the greater of m and 1. In practice, the upper limit for the summation is restricted to a value N_m where the near-field effects is shown to converge at $max(0.5ekd, a/x)$ with e as the natural logarithm [22].

Applying the boundary conditions in Eq. 4.1 and Eq. 4.2, we get,

$$C_{\eta m}^{lM} + u_\eta(a) \sum_{\nu=(m,1)}^{N_{max}} D_{\nu m}^{lM} A_{\eta m}^{\nu m}(-k_f d) + D_{\eta m}^{lN} B_{\eta m}^{\nu m}(-k_f d) = p_\eta^M \delta_{\eta l} \qquad (4.18)$$

$$C_{\eta m}^{lN} + \nu_\eta(a) \sum_{\nu=(m,1)}^{N_{max}} D_{\nu m}^{lM} B_{\eta m}^{\nu m}(-k_f d) + D_{\nu m}^{lN} A_{\eta m}^{\nu m}(-k_f d) = 0 \qquad (4.19)$$

$$D_{\eta m}^{lM} + u_\eta(b) \sum_{\nu=(m,1)}^{N_{max}} C_{\nu m}^{lM} A_{\eta m}^{\nu m}(+k_f d) + C_{\nu m}^{lN} B_{\eta m}^{\nu m}(+k_f d) = 0 \qquad (4.20)$$

$$D_{\eta m}^{lN} + \nu_\eta(b) \sum_{\nu=(m,1)}^{N_{max}} C_{\nu m}^{lM} B_{\eta m}^{\nu m}(+k_f d) + C_{\nu m}^{lN} A_{\eta m}^{\nu m}(+k_f d) = 0 \qquad (4.21)$$

Where η ranges from $(m, 1)$ to N_m and u_η and ν_η are the *Mie Coefficients* defined by,

$$u_\eta(a) = \frac{k_a \zeta_\eta^{(1)}(k_a a) z_\eta^{(1)}(k_f a) - k_f \zeta_\eta^{(1)}(k_f a) z_\eta^{(1)}(k_a a)}{k_a \zeta_\eta^{(1)}(k_a a) z_\eta^{(3)}(k_f a) - k_f \zeta_\eta^{(3)}(k_f a) z_\eta^{(1)}(k_a a)} \qquad (4.22)$$

$$\nu_\eta(a) = \frac{k_a \zeta_\eta^{(1)}(k_f a) z_\eta^{(1)}(k_f a) - k_f \zeta_\eta^{(1)}(k_a a) z_\eta^{(1)}(k_f a)}{k_a \zeta_\nu^{(1)}(k_f a) z_\eta^{(3)}(k_f a) - k_f \zeta_\nu^{(3)}(k_a a) z_\eta^{(1)}(k_f a)} \qquad (4.23)$$

For the scattered field due to $\vec{N}_{l,m}^{(3)}(k_a \vec{r}_a)$, the only difference is that the right hand side of Eq. 67 becomes 0 and the rhs of Eq. 68 becomes $p_\eta^N \delta_{\eta l}$

where p_η^M and p_η^N are defined as,

$$p_\eta^M = \frac{-i/(k_f a)}{k_a a \zeta_\eta^{(1)}(k_a a) z_\eta^{(3)}(k_f a) - k_f a \zeta_\eta^{(3)}(k_f a) z_\eta^{(1)}(k_a a)} \qquad (4.24)$$

$$p_\eta^N = \frac{-i/(k_f a)}{k_a a \zeta_\eta^{(3)}(k_f a) z_\eta^{(1)}(k_a a) - k_f a \zeta_\eta^{(1)}(k_a a) z_\eta^{(3)}(k_f a)} \qquad (4.25)$$

Once all the coefficients in Eq. 4.18 - 4.21 and the similar equations for the scattered field due to $\vec{N}_{l,m}^{(3)}(k_a \vec{r}_a)$, are obtained, the DGF due to scattering and its curl in Region C [22]:

$$\mathbf{G}_{sc}(r_a, r_a') = i k_f \sum_{\substack{l,\nu=(1,m) \\ m=-N_m}}^{\substack{m=N_m \\ l,\nu=N_m}} (-1)^m \left\{ \begin{bmatrix} C_{\nu m}^{lM} \vec{M}_{\nu m}^{(3)}(k_f r_a) + C_{\nu m}^{lN} \vec{N}_{\nu m}^{(3)}(k_f r_a) + \\ D_{\nu m}^{lM} \vec{M}_{\nu m}^{(3)}(k_f r_b) + D_{\nu m}^{lN} \vec{N}_{\nu m}^{(3)}(k_f r_b) \end{bmatrix} \vec{M}_{l,-m}^{(1)}(k_a r_a') \\ \begin{bmatrix} C_{\nu m}'^{lM} \vec{M}_{\nu m}^{(3)}(k_f r_a) + C_{\nu m}'^{lN} \vec{N}_{\nu m}^{(3)}(k_f r_a) + \\ D_{\nu m}'^{lM} \vec{M}_{\nu m}^{(3)}(k_f r_b) + D_{\nu m}'^{lN} \vec{N}_{\nu m}^{(3)}(k_f r_b) \end{bmatrix} \vec{N}_{l,-m}^{(1)}(k_a r_a') \right\}$$

$$(4.26)$$

$$\nabla \times \mathbf{G}_{sc}(r_a, r_a') = i k_f^2 \sum_{\substack{l,\nu=(1,m) \\ m=-N_m}}^{\substack{m=N_m \\ l,\nu=N_m}} (-1)^m \left\{ \begin{bmatrix} C_{\nu m}^{lM} \vec{N}_{\nu m}^{(3)}(k_f r_a) + C_{\nu m}^{lN} \vec{M}_{\nu m}^{(3)}(k_f r_a) + \\ D_{\nu m}^{lM} \vec{N}_{\nu m}^{(3)}(k_f r_b) + D_{\nu m}^{lN} \vec{M}_{\nu m}^{(3)}(k_f r_b) \end{bmatrix} \vec{M}_{l,-m}^{(1)}(k_a r_a') \\ \begin{bmatrix} C_{\nu m}'^{lM} \vec{N}_{\nu m}^{(3)}(k_f r_a) + C_{\nu m}'^{lN} \vec{M}_{\nu m}^{(3)}(k_f r_a) + \\ D_{\nu m}'^{lM} \vec{N}_{\nu m}^{(3)}(k_f r_b) + D_{\nu m}'^{lN} \vec{M}_{\nu m}^{(3)}(k_f r_b) \end{bmatrix} \vec{N}_{l,-m}^{(1)}(k_a r_a') \right\}$$

$$(4.27)$$

4.1.5   Radiative Heat Transfer

The radiative heat transfer between the two spheres is calculated from the Poynting vector normal to the surface of sphere B, which in turn depends on the tangential fields on the surface of sphere B. If the green function is determined for the configuration, the power can be calculated using Eq. 3.28.

$$\mathbf{G}_{sc}(r_a, r'_a) =$$

$$\frac{1}{b} \sum_{\substack{l,\nu=(1,m) \\ m=-N_m}}^{\substack{l,\nu=N_m \\ m=N_m}} (-1)^m \left\{ \begin{bmatrix} \left(\dfrac{-D_{\nu m}^{lM} z_l^{(1)}(k_b r_b)}{k_b b \zeta_\nu^{(1)}(k_b b) z_\nu^{(1)}(k_f b) - k_f b \zeta_\nu^{(1)}(k_f b) z_\nu^{(1)}(k_b b)} \right) V_{\nu m}^{(2)}(\theta_b, \phi_b) \\[2mm] \left(\dfrac{D_{\nu m}^{lN} \zeta_l^{(1)}(k_b r_b)}{k_b b \zeta_\nu^{(1)}(k_f b) z_\nu^{(1)}(k_b b) - k_f b \zeta_\nu^{(1)}(k_b b) z_\nu^{(1)}(k_f b)} \right) \vec{V}_{\nu m}^{(3)}(\theta_b, \phi_b) \\[2mm] \left(\dfrac{(k_b/k_f) D_{\nu m}^{lN} z_l^{(1)}(k_b r_b)(\sqrt{\nu(\nu+1)}/k_b b)}{k_b b \zeta_\nu^{(1)}(k_f b) z_\nu^{(1)}(k_b b) - k_f b \zeta_\nu^{(1)}(k_b b) z_\nu^{(1)}(k_f b)} \right) \vec{V}_{\nu m}^{(1)}(\theta_b, \phi_b) \end{bmatrix} \vec{M}_{l,-m}^{(1)}(k_a r'_a) \\[4mm] [similar\ terms\ with\ primed\ coefficients] \vec{N}_{l,-m}^{(1)}(k_a r'_a) \right\}$$

(4.28)

$$\nabla \times \mathbf{G}_{sc}(r_a, r'_a) =$$

$$\frac{k_f}{b} \sum_{\substack{l,\nu=(1,m) \\ m=-N_m}}^{\substack{l,\nu=N_m \\ m=N_m}} (-1)^m \left\{ \begin{bmatrix} \left(\dfrac{-(k_b/k_f) D_{\nu m}^{lM} \zeta_l^{(1)}(k_b r_b)}{k_b b \zeta_\nu^{(1)}(k_b b) z_\nu^{(1)}(k_f b) - k_f b \zeta_\nu^{(1)}(k_f b) z_\nu^{(1)}(k_b b)} \right) \vec{V}_{\nu m}^{(3)}(\theta_b, \phi_b) \\[2mm] \left(\dfrac{(k_b/k_f) D_{\nu m}^{lN} z_l^{(1)}(k_b r_b)}{k_b b \zeta_\nu^{(1)}(k_f b) z_\nu^{(1)}(k_b b) - k_f b \zeta_\nu^{(1)}(k_b b) z_\nu^{(1)}(k_f b)} \right) \vec{V}_{\nu m}^{(2)}(\theta_b, \phi_b) \\[2mm] \left(\dfrac{(k_b/k_f) D_{\nu m}^{lN} z_l^{(1)}(k_b r_b)(\sqrt{\nu(\nu+1)}/k_b b)}{k_b b \zeta_\nu^{(1)}(k_b b) z_\nu^{(1)}(k_f b) - k_f b \zeta_\nu^{(1)}(k_f b) z_\nu^{(1)}(k_b b)} \right) \vec{V}_{\nu m}^{(1)}(\theta_b, \phi_b) \end{bmatrix} \vec{M}_{l,-m}^{(1)}(k_a r'_a) \\[4mm] [similar\ terms\ with\ primed\ coefficients] \vec{N}_{l,-m}^{(1)}(k_a r'_a) \right\}$$

(4.29)

Finally, the net power transferred and the spectral radiative transfer between the two spheres respectively can be determined as [22]:

$$P(\omega; T_A, T_B) = \frac{a}{b} [\Theta(\omega, T_A) - \Theta(\omega, T_B)] \times$$

$$\sum_{m,l,\beta} \left\{ \begin{bmatrix} \Im\left(\dfrac{1}{x_\beta(b)}\right) \left| \dfrac{z_l^{(1)}(k_a a) D_{\beta m}^{lM}}{z_\beta^{(1)}(k_f b)} \right|^2 - \Im\left(\dfrac{1}{y_\beta(b))}\right) \left| \dfrac{z_l^{(1)}(k_a a) D_{\beta m}^{lN}}{z_\beta^{(1)}(k_f b)} \right|^2 \end{bmatrix} \Im\left(\dfrac{1}{x_l(a)}\right) |x_l(b)|^2 + \\[3mm] \begin{bmatrix} \Im\left(\dfrac{1}{x_\beta(b))}\right) \left| \dfrac{z_l^{(1)}(k_a a) D'^{lM}_{\beta m}}{z_\beta^{(1)}(k_f b)} \right|^2 - \Im\left(\dfrac{1}{y_\beta(b))}\right) \left| \dfrac{z_l^{(1)}(k_a a) D'^{lN}_{\beta m}}{z_\beta^{(1)}(k_f b)} \right|^2 \end{bmatrix} \Im\left(\dfrac{1}{y_l(a)}\right) |y_l(b)|^2 \right\}$$

(4.30)

$$G(\omega; T) = \lim_{T_A \to T_B} \frac{P(\omega, T_A, T_B)}{|T_A - T_B|} = k_B \left(\frac{\hbar\omega}{k_B T} \right)^2 \frac{e^{\hbar\omega/k_B T}}{(e^{\hbar\omega/k_B T} - 1)^2} \frac{a}{b} \times$$

$$\sum_{m,l,\beta} \left\{ \begin{matrix} \left[\Im\left(\frac{1}{x_\beta(b)}\right) \left| \frac{z_l^{(1)}(k_a a) D_{\beta m}^{lM}}{z_\beta^{(1)}(k_f b)} \right|^2 - \Im\left(\frac{1}{y_\beta(b))}\right) \left| \frac{z_l^{(1)}(k_a a) D_{\beta m}^{lN}}{z_\beta^{(1)}(k_f b)} \right|^2 \right] \Im\left(\frac{1}{x_l(a)}\right) |x_l(b)|^2 + \\ \left[\Im\left(\frac{1}{x_\beta(b))}\right) \left| \frac{z_l^{(1)}(k_a a) D_{\beta m}^{'lM}}{z_\beta^{(1)}(k_f b)} \right|^2 - \Im\left(\frac{1}{y_\beta(b))}\right) \left| \frac{z_l^{(1)}(k_a a) D_{\beta m}^{'lN}}{z_\beta^{(1)}(k_f b)} \right|^2 \right] \Im\left(\frac{1}{y_l(a)}\right) |y_l(b)|^2 \end{matrix} \right\} \quad (4.31)$$

4.2 Near-field Radiative Heat Transfer between Aluminum Nitride spheres

In the following, we compute the spectral conductance between two identical Aluminum Nitride spheres of radius a and gap x at 300K spanning a logarithmic scale over several orders of magnitude $[10nm, 10\mu m]$ highlighting the distinctive properties of near-field thermal radiation for the two sphere geometry as investigated by Narayanaswamy and Gang [22]. We, later, expand upon this discussion with optimizing radiative transfer modulation and coherence tuning. We present the results for a maximum radius to gap ratio of 17 for 800 frequency points over the spectrum from 0.0073 to 0.12 eV.

4.2.1 Contribution of Resonant Surface Waves

Conduction in the near-field limit for relatively small radii is dominated by surface phonon polariton regions showing maximal radiation at resonance frequencies. In Fig. 4.4 and 4.5, we plot the spectral conductance for various radii and gap combinations demonstrating resonance behavior typical of the two sphere geometry in the near-field limit thermal transfer for both defect states. The shift in the maximal conductance is in accordance with the resonance frequency regions for the different defect states of Aluminum Nitride as discussed in Chapter 2. The coherence signature of the AlN H-state is broader than that of the L-state as

predicted in Chapter 2.

4.2.2 Asymptotic Results for Near-Field Thermal Radiation

Unlike the near-field radiative transfer between two semi-infinite spaces which is determined by the gap (along the optical properties of the spaces and intervening medium) and similar to the the two thin film configuration [52], the radiative transfer for the two sphere configuration is determined by two length parameters and is a function of both the gap and the radius of the spheres. The near-field radiative transfer model proposed by Narayanaswamy and Gang is applicable for spheres of arbitrary radii and gaps and is only restricted by computational limitations. However, the asymptotic expressions for near-field thermal radiation for the limiting cases portrayed in Fig. 4.6 set a regime map for near-field radiative heat transfer, and thus NFRHT modulation and coherence tuning, for different radii and gaps combinations. We quantify the coherence of the near-field signal by the full-width at half maximum (FWHM) for the modes contributing to the near-field radiation in region corresponding to the reststrahlen band.

(i) **Proximity Theorem** $(x \ll a < \lambda)$**:**

For spheres separated by small gaps compared to the spheres radii, an asymptotic expression can be derived from the results of radiative transfer between two semi-infinite objects. Used for calculating Casimir and Van der Waals forces, this method is known as the proximity force theorem [53]. The proximity theorem is shown to be applicable for near-field thermal radiation with conductance varying linearly with a/x for spheres smaller than the radiation wavelength separated by small gaps $(x \ll a < \lambda)$ [22].
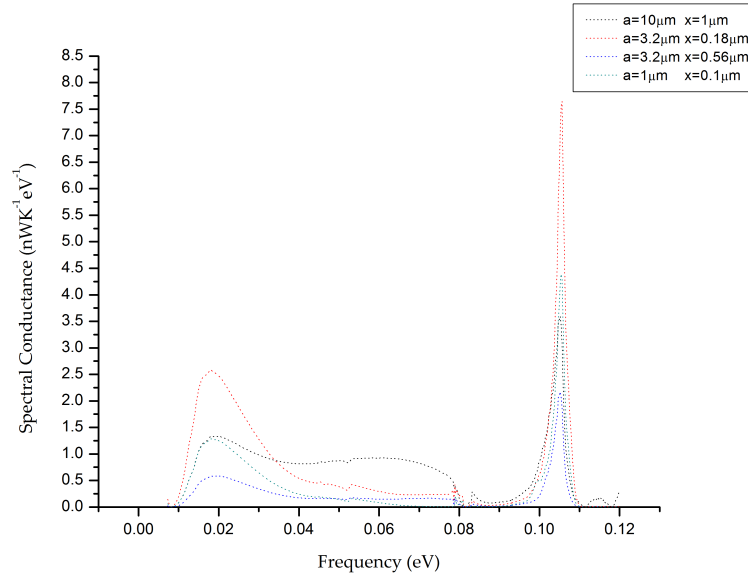
Figure 4.4: *Spectral Conductance for two Aluminum Nitride spheres of various radii and gaps in L-state*
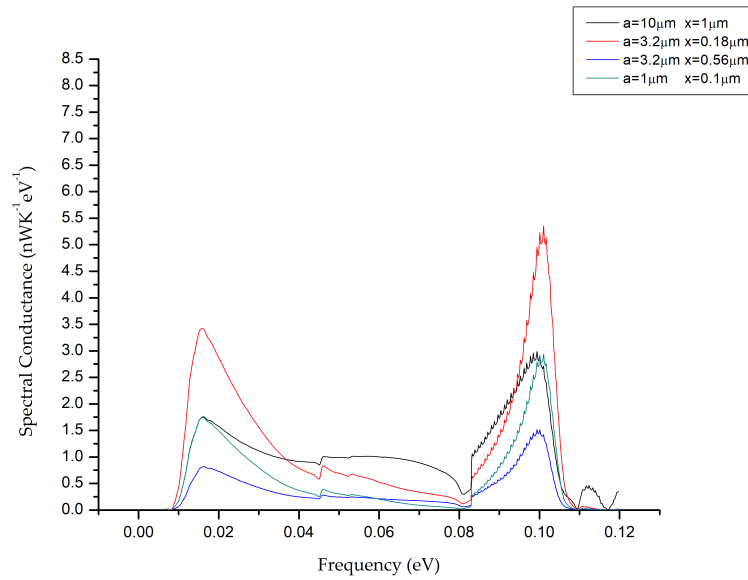

Figure 4.5: *Spectral Conductance for two Aluminum Nitride spheres of various radii and gaps in H-state*
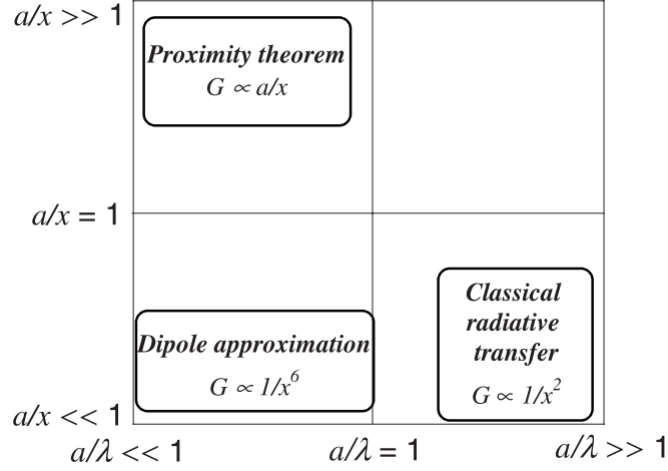
Figure 4.6: *Regime map for the two sphere problem. Radius of spheres is a, the gap between them is x, and the wavelength of radiation is λ*

In Fig. 4.7, we plot the spectral conductance between small spheres while maintaining the radius to gap ratios of $a/x = 10$ and 5.6 for both defect state of AlN. As predicted, the conductance of small spheres is identical for configurations of the same radius to gap ratio maintaining the same total conductance and coherence signature for configurations of constant radius to gap ratio.

However, for larger radii, the proximity theory is only approximate in the regions where electromagnetic waves dominate the heat transfer with increasing contribution from propagating waves where near-field radiative heat transfer is non-resonant for larger radii [22]. In Fig. 4.8, we plot the spectral conductance for spheres of large radius with the same radius to gap ratios for both defect states. We finally plot the spectral conductance as a function of the gap for both AlN defect states demonstrating the increase in the slope (with -1 corresponding to the proximity theorem) due to the increasing propagating modes contribution with increasing radius. Another feature of near-field transfer for the two sphere configuration
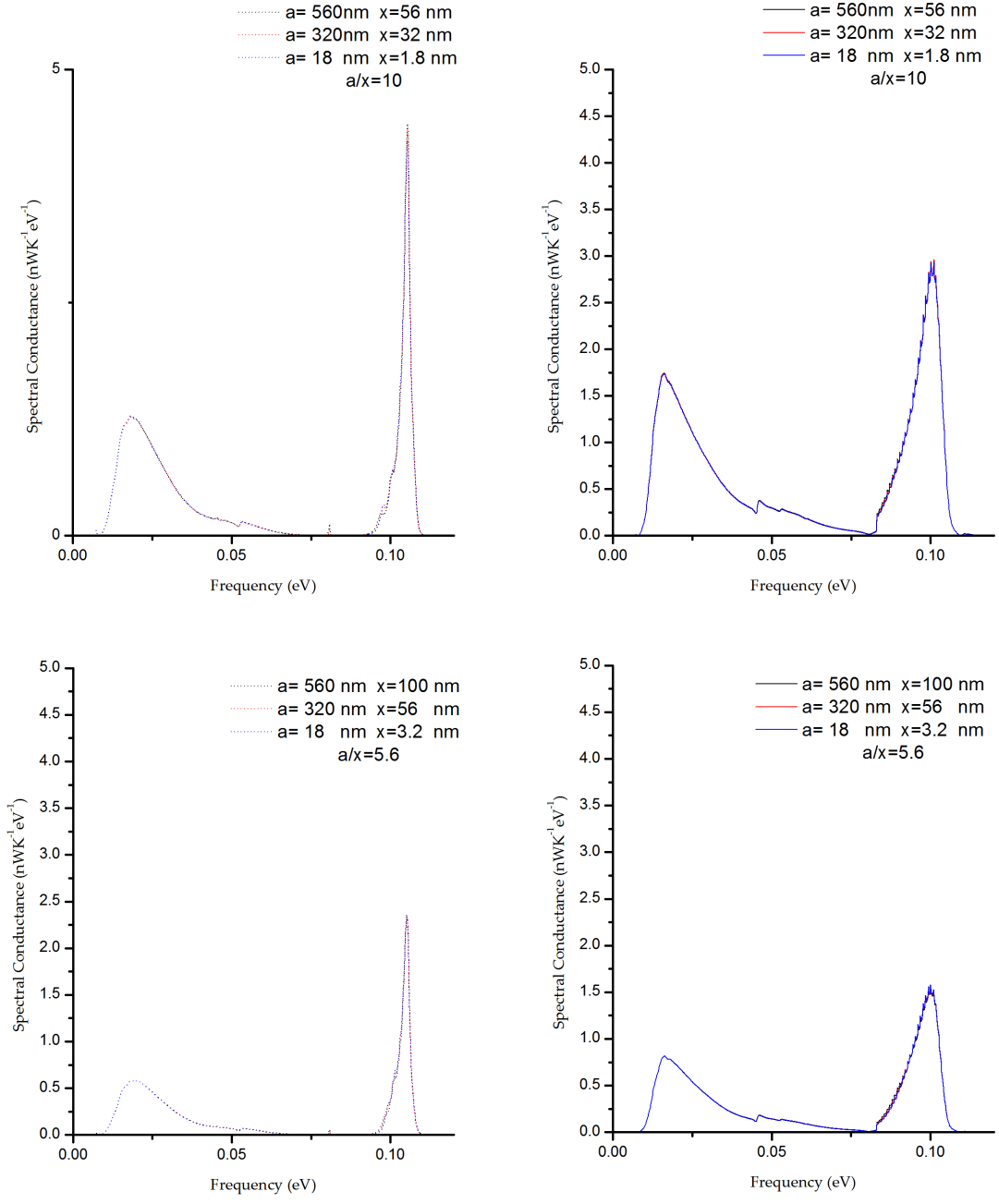
60

Figure 4.7: *Spectral Conductance of near-field transfer between spheres at radius to gap ratio of 10 (top) and 5.6 (bottom) for L-state (left) and H-state (right) for small radii ($a < \lambda$)*
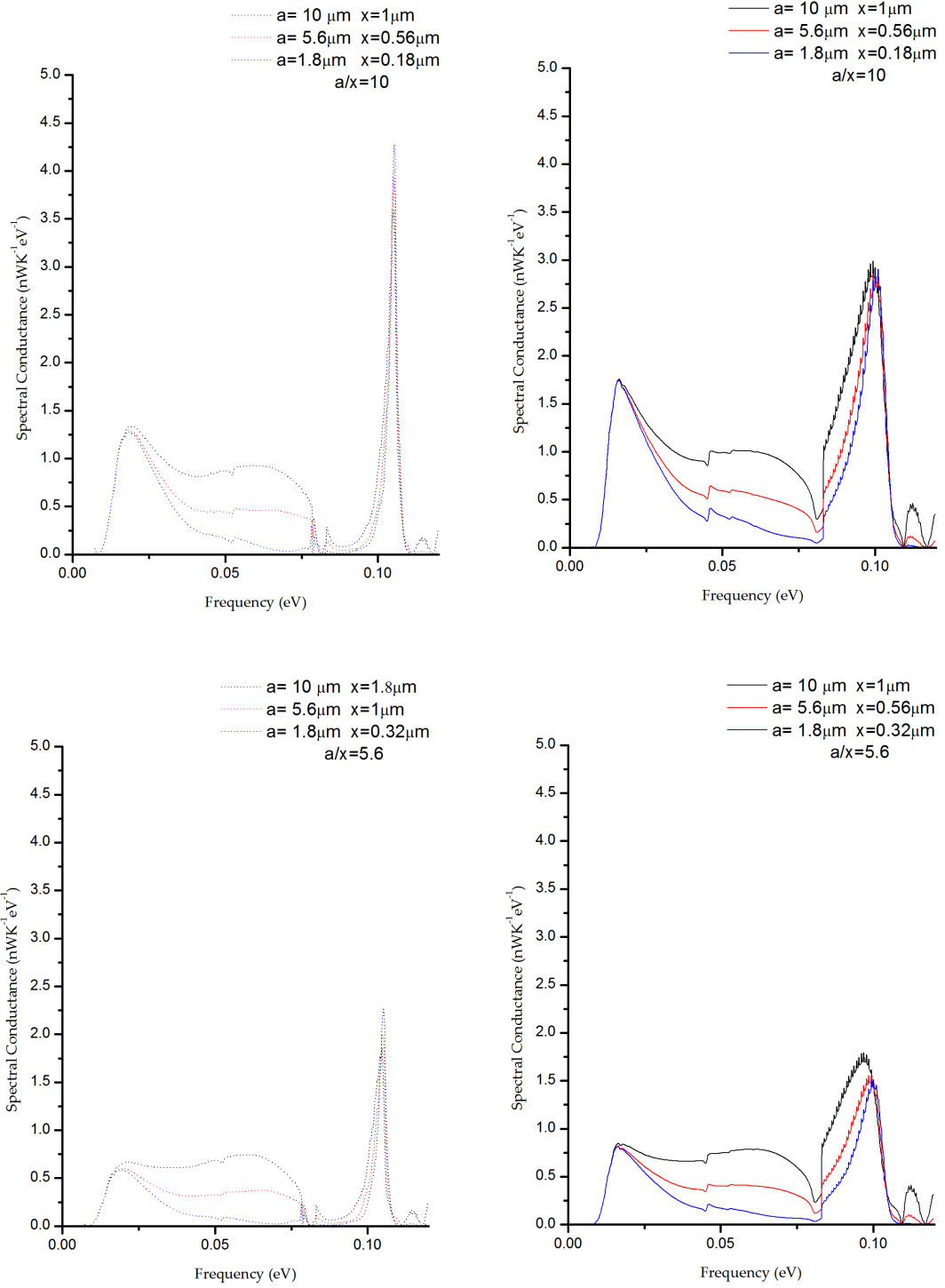
Figure 4.8: *Spectral conductance of near-field transfer between spheres at radius to gap ratio of 10 (top) and 5.6 (bottom) for L-state (left) and H-state (right) for large radii* ($a > \lambda$)
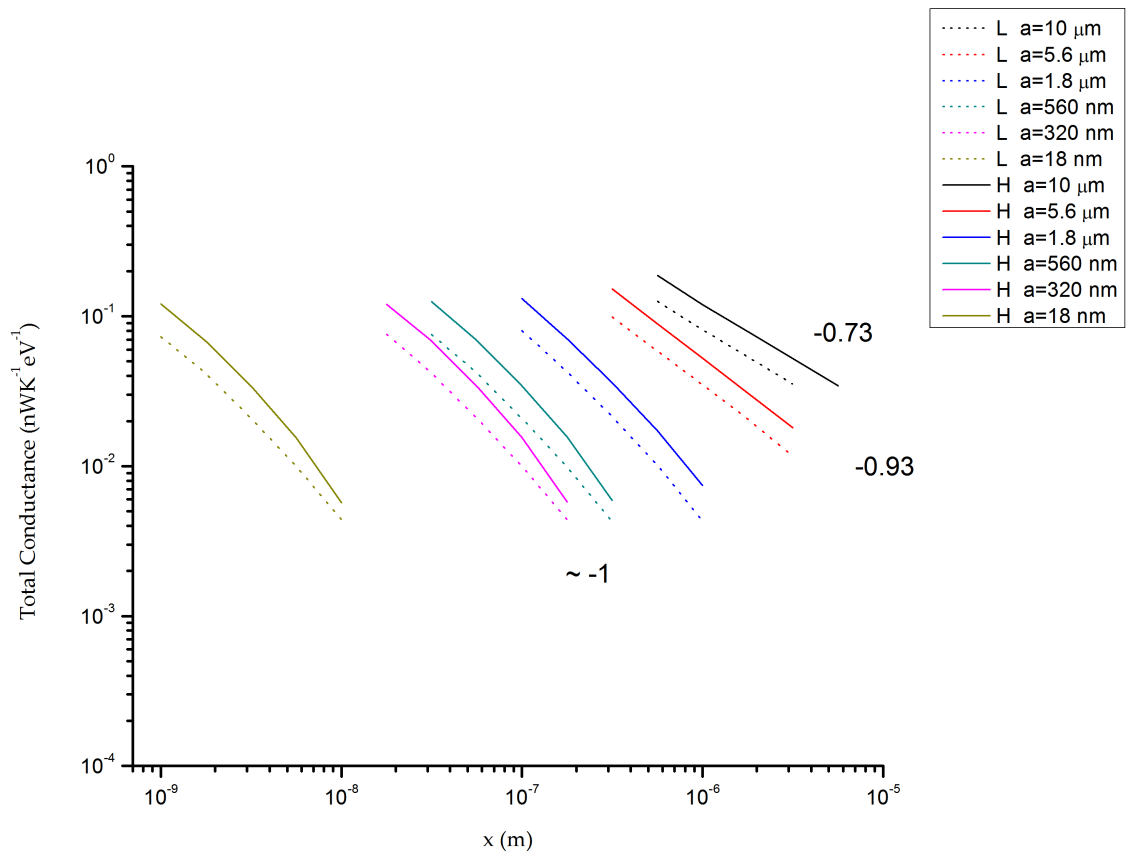
Figure 4.9: *Variation of total conductance with gap for L-state (dotted) and H-state (solid)*

is the increasing contribution of the propagating non-resonant modes that can potentially swamp the resonant radiative transfer as shown in Fig 4.11.

The similar resonance signatures for configurations of any constant a/x is a distinctive feature of the two sphere system. In the case of thin films, the invariance of the near-field heat transfer between two identical thin films for a certain ratio of the film thickness to the vacuum gap (t_f/d) is only valid for $t_f/d \leq 1$ [54].

In Fig. 4.10, we plot the corresponding FWHM of the simulated near-field spectra of radius to gap ratios of 10 (black) and 5.6 (red) for both defect states of AlN. We note that the coherence signature for small radii maintains the same FWHM for a constant radius to gap ratio in accordance with proximity theory. However, for larger radii, the FWHM increases with increasing non-resonant modes contribution.

(ii) **Dipole Approximation** ($a \ll \lambda\ and\ a \ll x \ll \lambda$):

For very small spheres of radii much smaller than the thermal wavelength, the spheres can be treated as point dipoles and the conductance between the spheres is given by the *dipole approximation* [55] with conductance varying as $1/x^6$ [22]. In Fig. 4.12, we plot the total conductance for L-state (the H-state follows the same trend by an almost fixed offset as investigated later) for spheres of radii with gaps spanning several orders of magnitude highlighting the transition from the proximity theorem (with a slope of approximately -1) to the dipole approximation (with a slope of approximately -6). We also note the gradual transition towards the classical radiative transfer regime with a slope of zero.
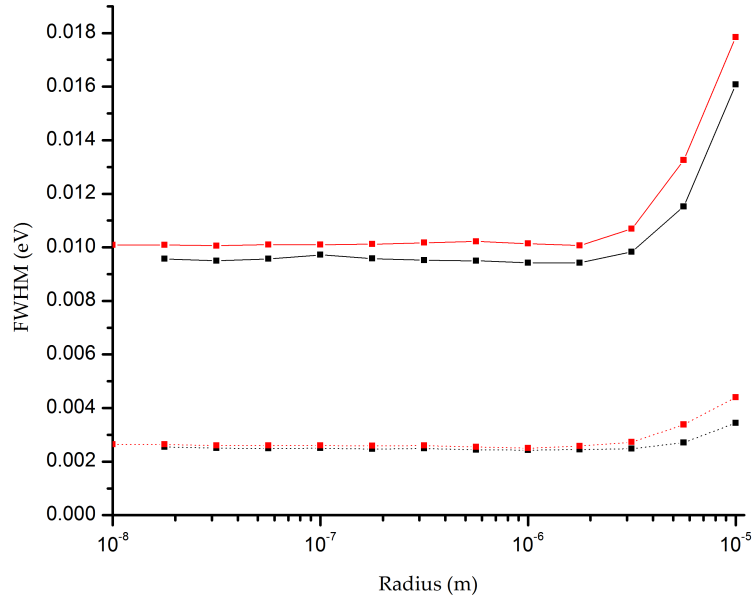
Figure 4.10: *Variation of FWHM with radius for configurations of constant radius to gap ratio*
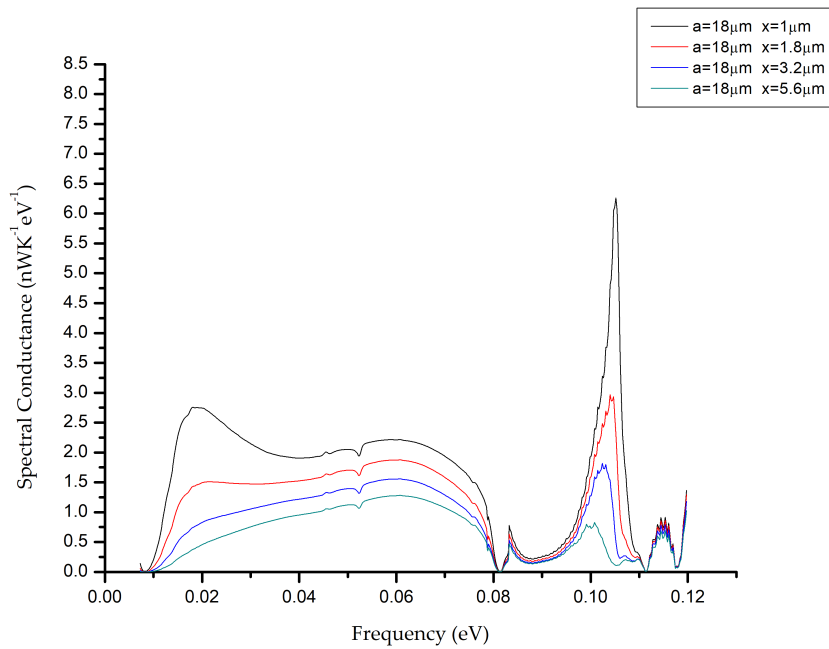

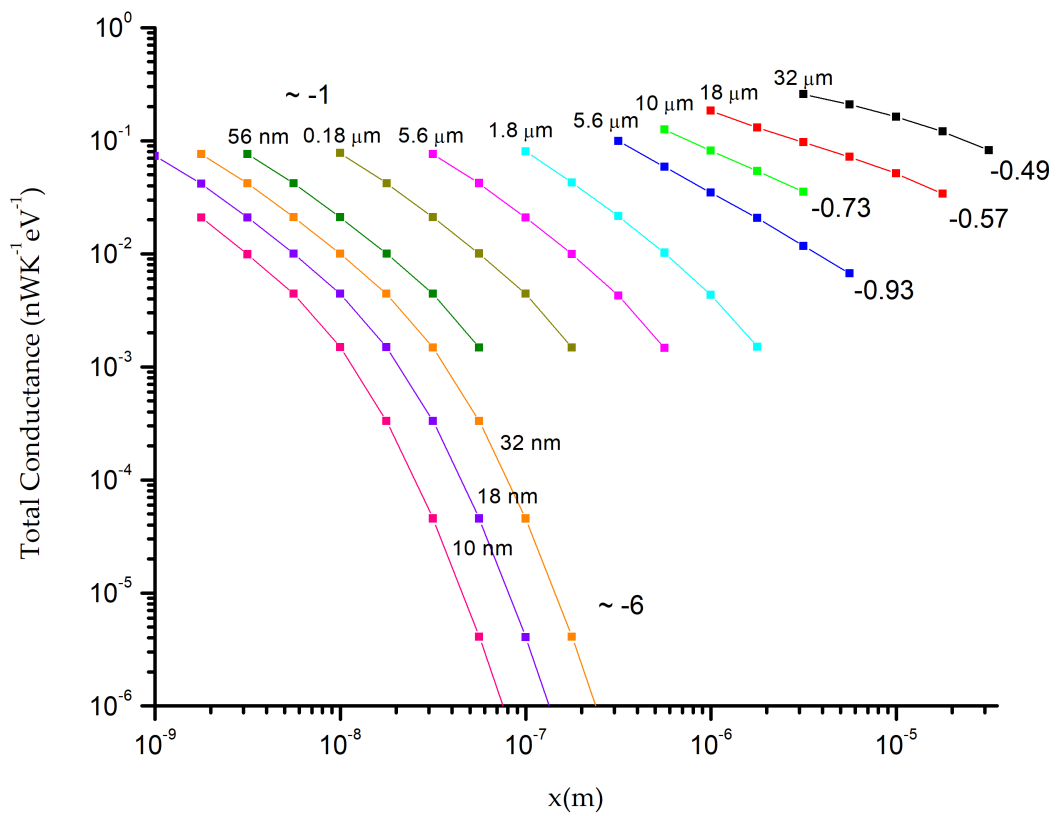Figure 4.11: *Spectral Conductance of 18 μm AlN spheres in L-state*

65

Figure 4.12: *Variation of total conductance with gap for spheres of radii of several orders of magnitude*
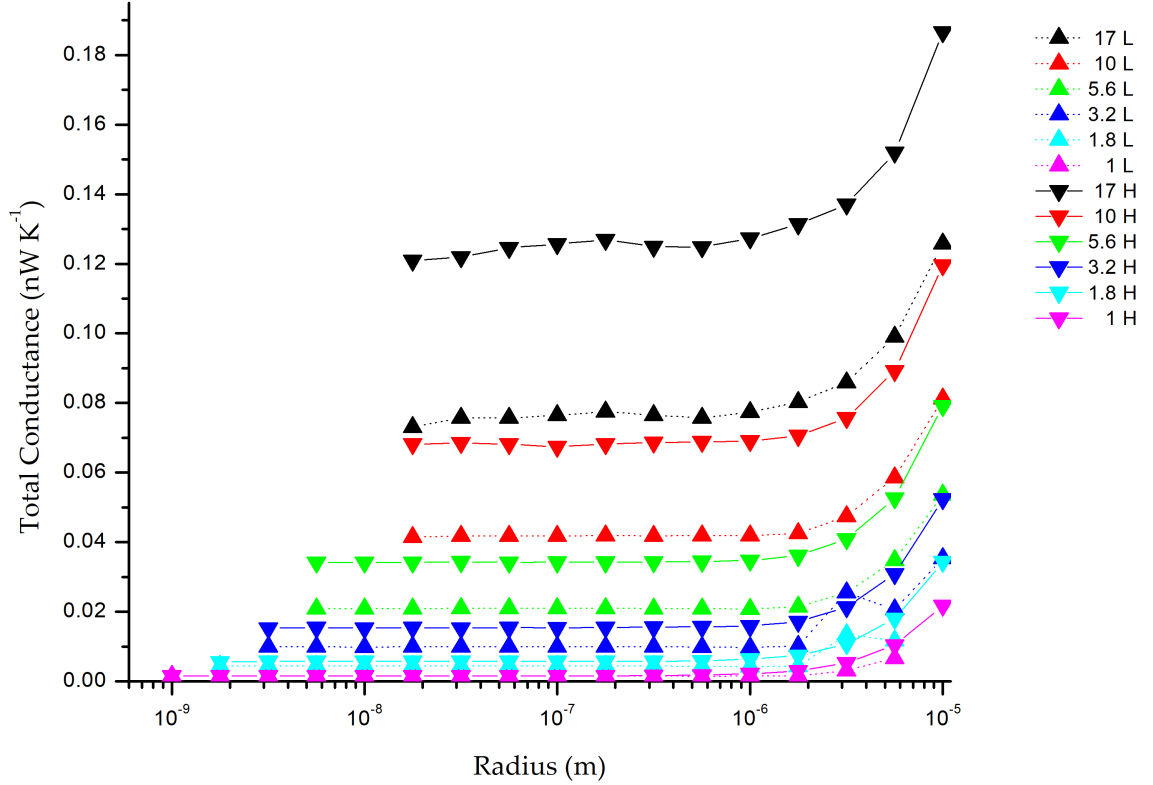
Figure 4.13: *Variation of total conductance with radius for configurations of constant radius to gap ratio for L-state (dotted) and H-state (solid)*

4.3 Tuning of Near-field Radiation

In this section, we investigate near-field conductance modulation by harnessing the transition between the two defect states of AlN for various radii and gap combinations. The conductance for the dipole approximation limit as displayed in Fig. 4.12 is negligible for all radii in comparison with the proximity theorem limit and drops rapidly with gap. Therefore, we consider the proximity theorem limit ($x \ll a$) where the conductance is appreciable for near-field modulation and coherence tuning.
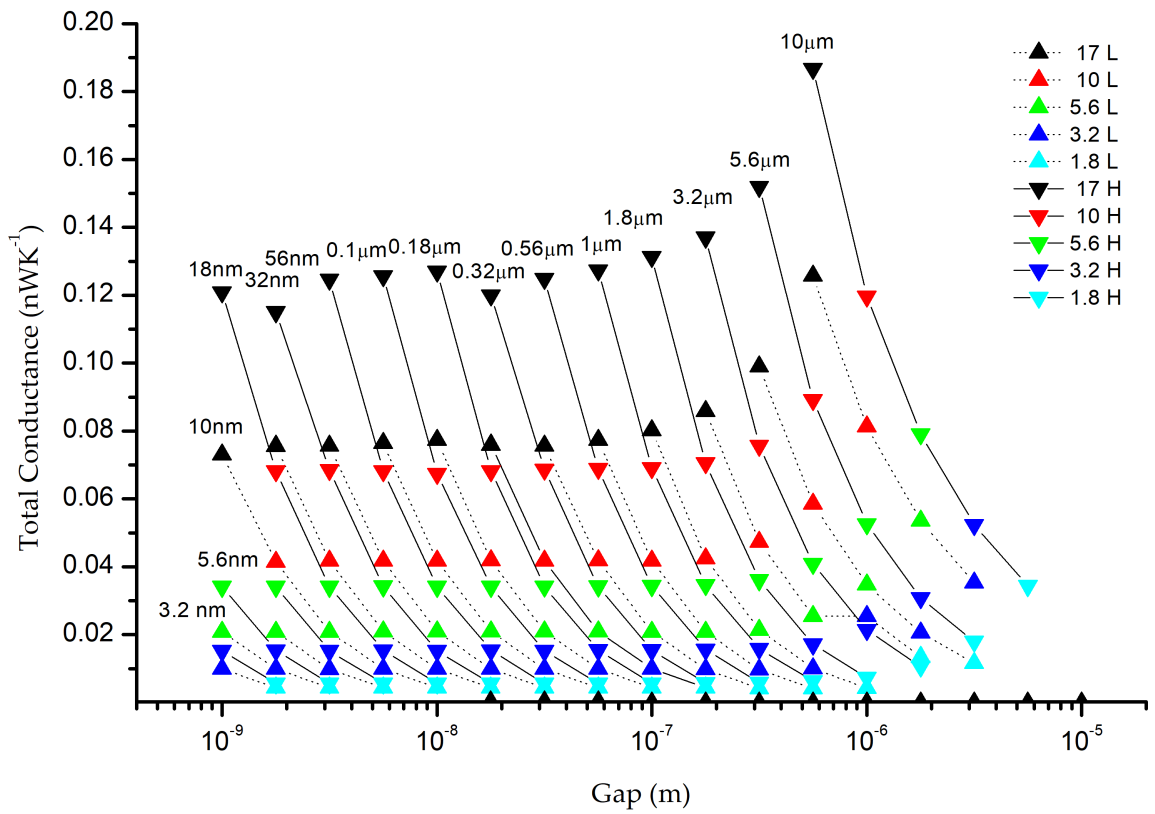
Figure 4.14: *Variation of total conductance with gap for spheres of radii of several orders of magnitude. Colors correspond to constant radius to gap ratio configurations*

Distinctive to the two sphere geometry, the similarity in resonance signature for a constant radius to gap ratio for small radii can be harnessed for modulating near-field radiation with the same on-off ratio for any configuration with the same radius to gap ratio. In Fig. 4.13, we plot the total conductance for both defect states of AlN for radii spanning several orders of magnitude $[10^{-9}, 10^{-5}]$ for different radius to gap ratios for both defect states of AlN. The conductance of small radii ($a < \lambda$) as displayed in Fig. 4.13 and 4.14 is constant for all configurations of the same radius to gap ratio. For larger radii, the conductance increases due to the non-resonant modes contribution as displayed in Fig. 4.8. Accordingly, the ratio of conductance for the H-state to the L-state is constant for the same radius to gap ratio for small radii as displayed in Fig. 4.15. The highest ratio attained in the investigated radius gap combinations spanning the orders $[10^{-9}, 10^{-5}]$ up to the radius to gap ratio of 17 in the small radius limit is 1.64 thus accordingly a modulation of 39%. In Fig. 4.16, we plot the example of the spectral conductance for a $100nm$ sphere separated by gaps for the different sphere to gap ratios investigated displaying an increasing modulation of the integrated area with increasing radius to gap ratio. The ratio further becomes constant at high radius to gap ratio where the two sphere system is effectively in the limit of the two parallel plate system where modulation ratio is close to 1.6, thus a modulation of 37%, for all gaps in the near-field limit as demonstrated in Chapter 3. For larger radii, the ratio fluctuates and becomes unpredictable with further increase in radius.

In terms of coherence tuning, we plot in Fig. 4.17 the corresponding FWHM for the configurations displayed in Fig. 4.14 along with the ratio of FWHM upon switching defect state in Fig. 4.18. The similarity of the resonance signature for configurations of the same radius to gap ratio for small radii shows up as a

69
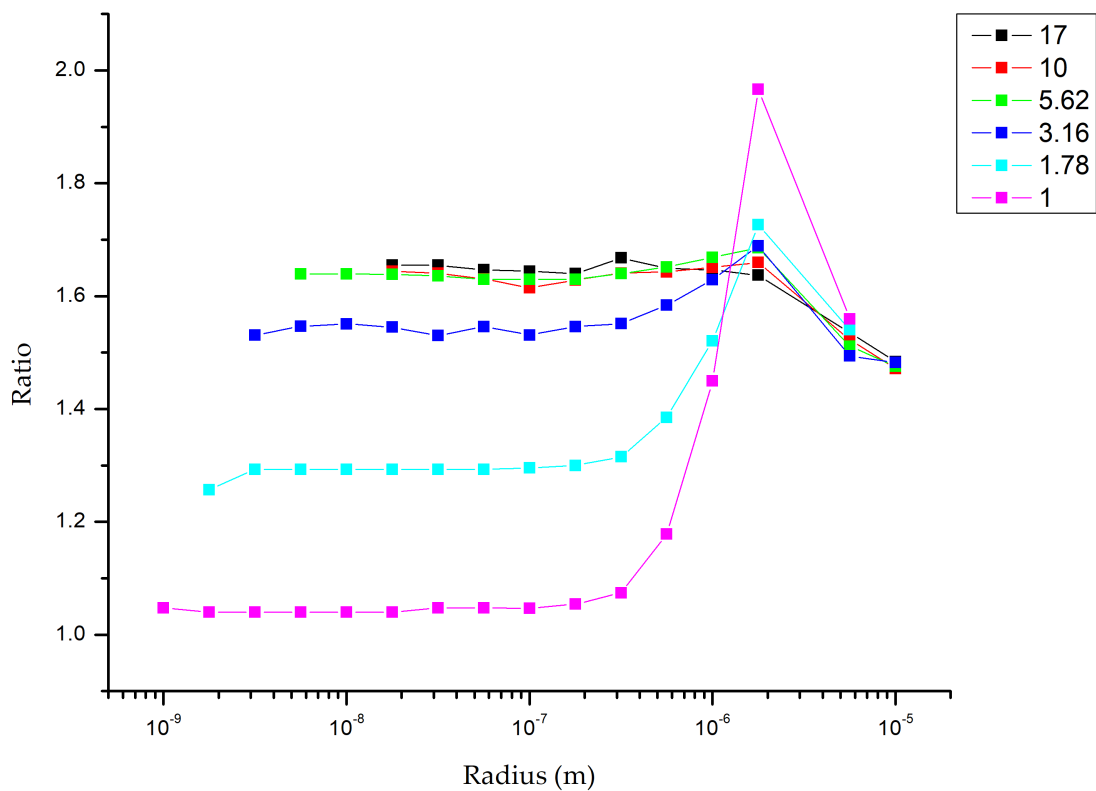
Figure 4.15: *Variation of total conductance ratio between AlN defect states for configurations of constant radius to gap ratio*
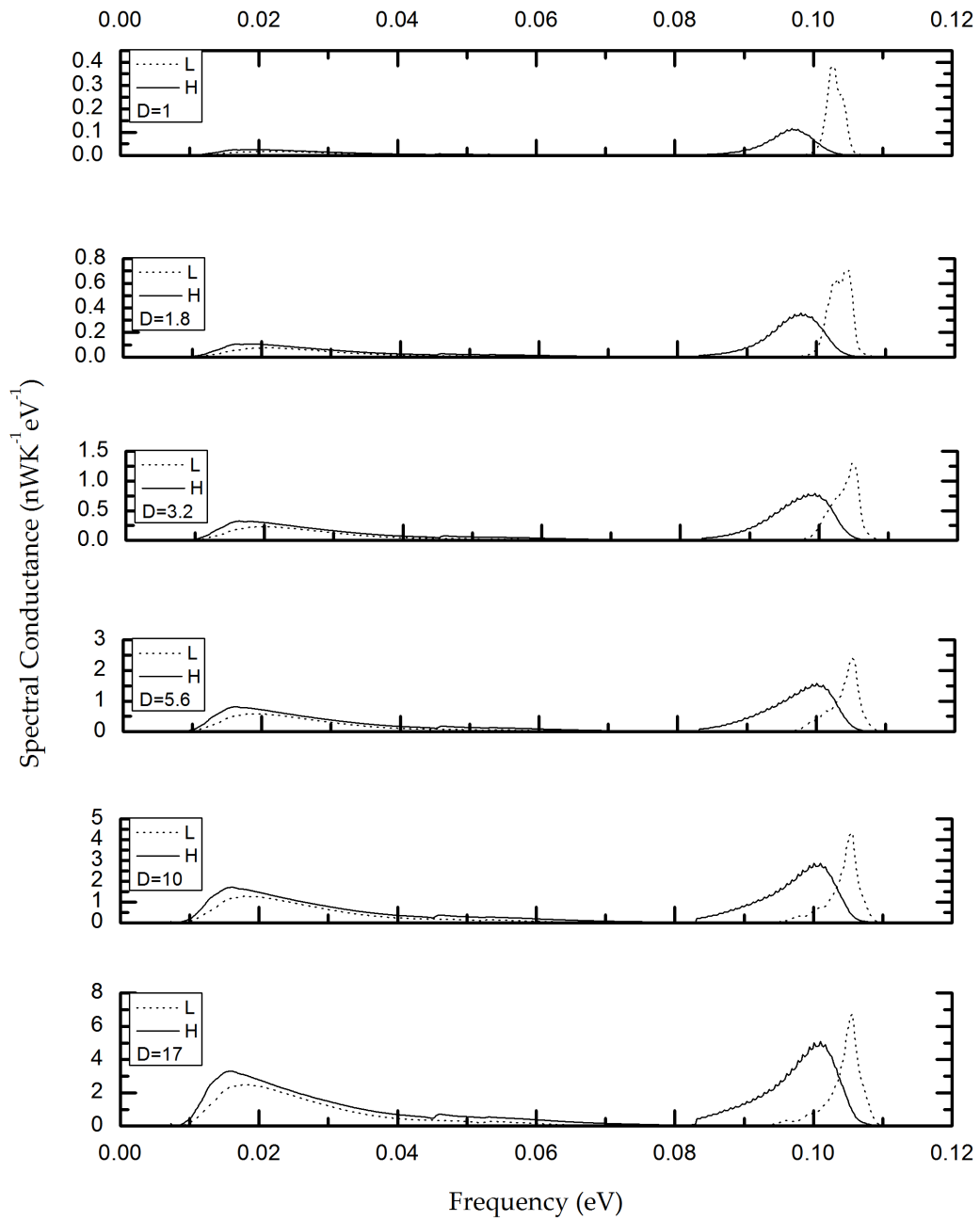
Figure 4.16: *Variation of Spectral Conductance with gap to radius ratio (a=100nm)*
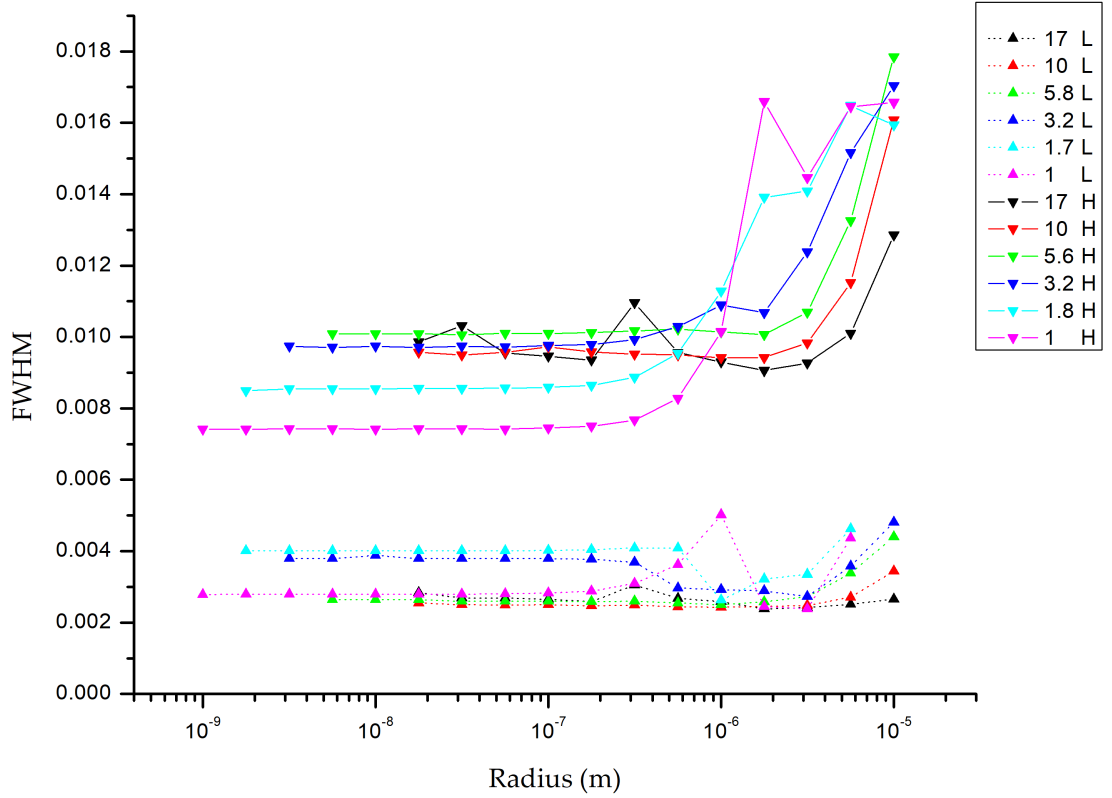
Figure 4.17: *Variation of FWHM with radius for configurations of constant radius to gap ratio for AlN defect states*

constant FWHM for configurations with constant ratio. Coherence can therefore be tuned by the same factor for configurations with the same radius to gap ratio in the small radius limit as displayed in Fig. 4.18. The FHWM ratio increases with increasing radius to gap ratio until it converges to the parallel plate limit close to 3.7 as demonstrated in Chapter 3.

Figure 4.18: *Variation of FHWM Ratio between AlN defect states for configurations of constant radius to gap ratio*

Chapter 5

Conclusion

In this dissertation, we have investigated the change in near-field radiative thermal transfer between parallel plates at different gaps upon switching between AlN defect states. A 36% modulation has been predicted for the net thermal transfer coefficient between the parallel plates along with a factor of 3.7 in FWHM in the spectral conductance resonance peak. We further investigated the radiative 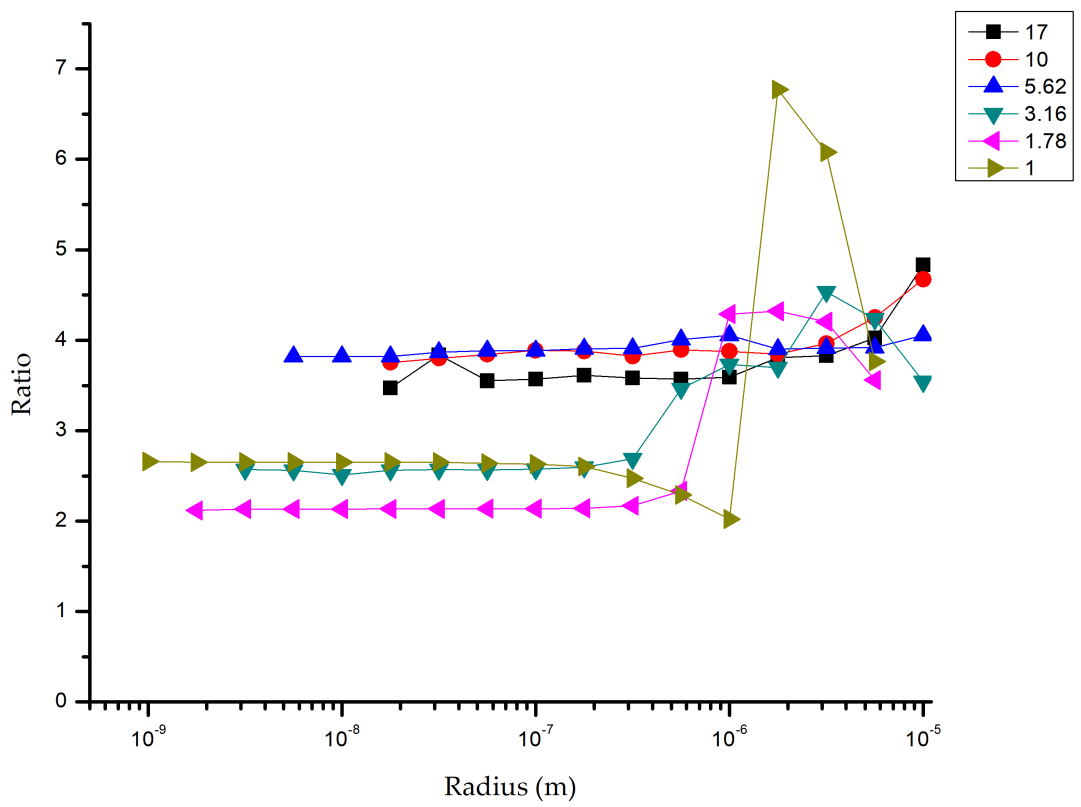thermal transfer in the two spheres geometry. Upon introducing a second length parameter in the problem, the thermal transfer between the two spheres show distinct properties including resonance conditions, net thermal transfer dependence on both length parameters along with the associated regime map for net thermal conductance variation, as well as resonance sweeping features critical for large spheres. The dimensionless parameters of radius to gap ratio as well as the radius to thermal wavelength ratio, which determines the far to near-field transition, are crucial for determining the near-field thermal transfer variation along with the associated different asymptotic limits. The variation of the spectral conductance for the two sphere problem has been computed until a convergence to the two plate geometry limit has been observed with a 39% modulation along

with a 3.7 FWHM ratio upon switching between AlN defect states.

The capability of manipulating electric currents is pivotal for the functioning of diodes, transistors, as well as major building blocks of electronics. Inspired by the ability of electronic devices to manipulate electrical currents, several attempts for theorizing an efficient thermal analogue operating in the near-field have been employed mostly via harnessing the properties of phase-change materials. For instance, the asymmetry of the heat flux exchanged between the two terminals of the diode with reversing temperature differences is possible due to the phase change properties of PCMs switching between temperatures above and bellow the critical temperature. Accordingly, a photonic thermal transistor was rendered possible along with the transistors combinations functioning as memory devices and logic gates. The capability behind tuning near-field radiative transfer is the key working principle for the recently proposed thermal devices operating in the near-field regime.

In this dissertation, we have introduced piezoelectrics as a new class of materials for near-field radiative transfer by investigating the near-field limit infrared radiation of AlN. With its fast response and sensitivity to electric field, detecting a defect state change in the infrared optical properties of AlN renders the possibility of electrically modulating near-field radiation at any temperature. This flexibility in tuning near-field radiation is promising for applications for near-field control essential for the current attempts for realizing thermal alternative to electronic systems. Typical PCM materials harnessed in applications of near-field tuning so far operate at cryogenic or room temperatures. Therefore, the operation of the corresponding thermal devices relies on temperature-dependent material properties, which limit their operating temperature range. For devices functioning at higher temperatures, new materials are needed. In fact, the ther-

mal photonic alternative to electronics is essentially proposed to operate under harsh environments associated with high temperatures where electronics typically fail. For instance, electronics degrade at high temperatures and fail in applications of high temperature environment space exploration (e.g. Venus) and high geothermal temperature investigations.

Very recent attempts have been concerned with high temperature near-field thermal transfer modulation. The gap separation sensitivity of near-field thermal radiation has been lately harnessed by ElZouka in proposing, fabricating, and testing of a proof-of-concept NanoThermoMechanical device that has shown a maximum rectification of 10.9% at terminals' temperatures of 375 and 530K; the functioning of the device was tested at temperatures as high as 600K [56]. Harnessing the defect state change at high temperature, can render AlN useful for tuning near-field radiative transfer at high temperatures where other methods of tuning near-field thermal radiation at constant gap separation fail. Therefore, we expect that our results will provide a highly needed tool for tailoring near-field radiative transfer with an external electric field and help to gain insight into the application of defect engineering in near-field nanophotonics.

Bibliography

[1] Z. M. Zhang, *Nano/microscale heat transfer.* No. Sirsi) i9780071436748, 2007.

[2] S. M. Rytov, "Theory of electric fluctuations and thermal radiation," tech. rep., AIR FORCE CAMBRIDGE RESEARCH LABS HANSCOM AFB MA, 1959.

[3] J.-P. Mulet, K. Joulain, R. Carminati, and J.-J. Greffet, "Enhanced radiative heat transfer at nanometric distances," *Microscale Thermophysical Engineering*, vol. 6, no. 3, pp. 209–222, 2002.

[4] B. Li, L. Wang, and G. Casati, "Negative differential thermal resistance and thermal transistor," *Applied Physics Letters*, vol. 88, no. 14, p. 143501, 2006.

[5] L. Wang and B. Li, "Thermal logic gates: computation with phonons," *Physical review letters*, vol. 99, no. 17, p. 177208, 2007.

[6] N. Li, J. Ren, L. Wang, G. Zhang, P. Hänggi, and B. Li, "Colloquium: Phononics: Manipulating heat flow with electronic analogs and beyond," *Reviews of Modern Physics*, vol. 84, no. 3, p. 1045, 2012.

[7] P. Ben-Abdallah and S.-A. Biehs, "Thermotronics: Towards nanocircuits to manage radiative heat flux," *Zeitschrift für Naturforschung A*, vol. 72, no. 2, pp. 151–162, 2017.

[8] P. Ben-Abdallah and S.-A. Biehs, "Near-field thermal transistor," *Physical review letters*, vol. 112, no. 4, p. 044301, 2014.

[9] C. R. Otey, W. T. Lau, S. Fan, *et al.*, "Thermal rectification through vacuum," *Physical Review Letters*, vol. 104, no. 15, p. 154301, 2010.

[10] P. Ben-Abdallah and S.-A. Biehs, "Towards boolean operations with thermal photons," *Physical Review B*, vol. 94, no. 24, p. 241401, 2016.

[11] V. Kubytskyi, S.-A. Biehs, and P. Ben-Abdallah, "Radiative bistability and thermal memory," *Physical review letters*, vol. 113, no. 7, p. 074301, 2014.

[12] S.-A. Biehs, F. S. Rosa, and P. Ben-Abdallah, "Modulation of near-field heat transfer between two gratings," *Applied Physics Letters*, vol. 98, no. 24, p. 243102, 2011.

[13] A. W. Rodriguez, M. T. H. Reid, and S. G. Johnson, "Fluctuating-surface-current formulation of radiative heat transfer for arbitrary geometries," *Phys. Rev. B*, vol. 86, p. 220302, Dec 2012.

[14] A. I. Volokitin and B. N. J. Persson, "Theory of the interaction forces and the radiative heat transfer between moving bodies," *Phys. Rev. B*, vol. 78, p. 155437, Oct 2008.

[15] G. Dedkov and A. Kyasov, "Conservative–dissipative forces and heating mediated by fluctuation electromagnetic field: Two plates in relative nonrelativistic motion," *Surface Science*, vol. 604, no. 5-6, pp. 562–567, 2010.

[16] L. Cui, Y. Huang, and J. Wang, "Near-field radiative heat transfer between chiral metamaterials," *Journal of Applied Physics*, vol. 112, no. 8, p. 084309, 2012.

[17] Y. Huang, S. V. Boriskina, and G. Chen, "Electrically tunable near-field radiative heat transfer via ferroelectric materials," *Applied Physics Letters*, vol. 105, no. 24, p. 244102, 2014.

[18] P. Van Zwol, K. Joulain, P. B. Abdallah, J.-J. Greffet, and J. Chevrier, "Fast nanoscale heat-flux modulation with phase-change materials," *Physical Review B*, vol. 83, no. 20, p. 201404, 2011.

[19] P. Van Zwol, K. Joulain, P. Ben-Abdallah, and J. Chevrier, "Phonon polaritons enhance near-field thermal transfer across the phase transition of vo 2," *Physical Review B*, vol. 84, no. 16, p. 161413, 2011.

[20] L. Zhu, C. R. Otey, and S. Fan, "Ultrahigh-contrast and large-bandwidth thermal rectification in near-field electromagnetic thermal transfer between nanoparticles," *Physical Review B*, vol. 88, no. 18, p. 184301, 2013.

[21] M. Nikbakht, "Radiative heat transfer in anisotropic many-body systems: Tuning and enhancement," *Journal of Applied Physics*, vol. 116, no. 9, p. 094307, 2014.

[22] A. Narayanaswamy and G. Chen, "Thermal near-field radiative transfer between two spheres," *Physical Review B*, vol. 77, no. 7, p. 075125, 2008.

[23] T. Mattila and R. M. Nieminen, "Ab initio study of oxygen point defects in gaas, gan, and aln," *Physical Review B*, vol. 54, no. 23, p. 16676, 1996.

[24] Q. Hu, T. Noda, H. Tanigawa, T. Yoneoka, and S. Tanaka, "The oxygen-related defect complexes in aln under gamma irradiation and quantum chemistry calculation," *Nuclear Instruments and Methods in Physics Research Section B: Beam Interactions with Materials and Atoms*, vol. 191, no. 1-4, pp. 536–539, 2002.

[25] R. A. Youngman and J. H. Harris, "Luminescence studies of oxygen-related defects in aluminum nitride," *Journal of the American Ceramic Society*, vol. 73, no. 11, pp. 3238–3246, 1990.

[26] L. E. McNeil, M. Grimsditch, and R. H. French, "Vibrational spectroscopy of aluminum nitride," *Journal of the American Ceramic Society*, vol. 76, no. 5, pp. 1132–1136, 1993.

[27] C. Yeh and F. I. Shimabukuro, *The essence of dielectric waveguides.* Springer, 2008.

[28] A. I. Volokitin and B. N. Persson, "Electromagnetic fluctuations at the nanoscale," 2017.

[29] S. Ancey, Y. Décanini, A. Folacci, and P. Gabrielli, "Surface plasmon polaritons and surface phonon polaritons on metallic and semiconducting spheres: Exact and semiclassical descriptions," *JOSA B*, vol. 26, no. 6, pp. 1176–1187, 2009.

[30] C. F. Bohren and D. R. Huffman, *Absorption and scattering of light by small particles.* John Wiley & Sons, 2008.

[31] W. Greiner, L. Neise, and H. Stöcker, *Thermodynamics and statistical mechanics.* Springer Science & Business Media, 2012.

[32] A. C. Jones, B. T. O'Callahan, H. U. Yang, and M. B. Raschke, "The thermal near-field: coherence, spectroscopy, heat-transfer, and optical forces," *Progress in Surface Science*, vol. 88, no. 4, pp. 349–392, 2013.

[33] E. G. Cravalho, C. L. Tien, and R. Caren, "Effect of small spacings on radiative transfer between two dielectrics," *Journal of Heat Transfer*, vol. 89, no. 4, pp. 351–358, 1967.

[34] R. Boehm and C. Tien, "Small spacing analysis of radiative transfer between parallel metallic surfaces," *Journal of Heat Transfer*, vol. 92, no. 3, pp. 405–411, 1970.

[35] J. L. Pan, H. K. Choy, and C. Fonstad, "Very large radiative transfer over small distances from a black body for thermophotovoltaic applications," *IEEE Transactions on Electron Devices*, vol. 47, no. 1, pp. 241–249, 2000.

[36] S. Basu, B. J. Lee, and Z. Zhang, "Near-field radiation calculated with an improved dielectric function model for doped silicon," *Journal of Heat Transfer*, vol. 132, no. 2, p. 023302, 2010.

[37] D. Polder and M. Van Hove, "Theory of radiative heat transfer between closely spaced bodies," *Physical Review B*, vol. 4, no. 10, p. 3303, 1971.

[38] J. D. Jackson, *Classical electrodynamics*. Wiley, 1999.

[39] M. Francoeur and M. P. Mengüç, "Role of fluctuational electrodynamics in near-field radiative heat transfer," *Journal of Quantitative Spectroscopy and Radiative Transfer*, vol. 109, no. 2, pp. 280–293, 2008.

[40] G. Kristensson, *Scattering of electromagnetic waves by obstacles*. The Institution of Engineering and Technology, 2016.

[41] G. Bimonte, T. Emig, M. Kardar, and M. Krüger, "Nonequilibrium fluctuational quantum electrodynamics: Heat radiation, heat transfer, and force," *Annual Review of Condensed Matter Physics*, vol. 8, pp. 119–143, 2017.

[42] L. D. Landau, J. Bell, M. Kearsley, L. Pitaevskii, E. Lifshitz, and J. Sykes, *Electrodynamics of continuous media*, vol. 8. elsevier, 2013.

[43] K. Joulain, R. Carminati, J.-P. Mulet, and J.-J. Greffet, "Definition and measurement of the local density of electromagnetic states close to an interface," *Physical Review B*, vol. 68, no. 24, p. 245405, 2003.

[44] M. Francoeur, *Near-field radiative transfer: Thermal radiation, thermophotovoltaic power generation and optical characterization.* University of Kentucky, 2010.

[45] K. Joulain, J.-P. Mulet, F. Marquier, R. Carminati, and J.-J. Greffet, "Surface electromagnetic waves thermally excited: Radiative heat transfer, coherence properties and casimir forces revisited in the near field," *Surface Science Reports*, vol. 57, no. 3-4, pp. 59–112, 2005.

[46] C. Fu and Z. Zhang, "Nanoscale radiation heat transfer for silicon at different doping levels," *International Journal of Heat and Mass Transfer*, vol. 49, no. 9-10, pp. 1703–1718, 2006.

[47] T. Rother and M. Kahnert, *Electromagnetic wave scattering on nonspherical particles.* Springer, 2009.

[48] O. R. Cruzan, "Translational addition theorems for spherical vector wave functions," *Quarterly of Applied Mathematics*, vol. 20, no. 1, pp. 33–40, 1962.

[49] W. Chew, "Recurrence relations for three-dimensional scalar addition theorem," *Journal of Electromagnetic Waves and Applications*, vol. 6, no. 1-4, pp. 133–142, 1992.

[50] W. C. Chew and Y. Wang, "Efficient ways to compute the vector addition theorem," *Journal of Electromagnetic Waves and Applications*, vol. 7, no. 5, pp. 651–665, 1993.

[51] C. Tai, *Dyadic Green's functions in electromagnetic theory*. Intext Monograph Series in Electrical Engineering, Intext Educational Publishers, 1971.

[52] S.-A. Biehs, D. Reddig, and M. Holthaus, "Thermal radiation and near-field energy density of thin metallic films," *The European Physical Journal B*, vol. 55, no. 3, pp. 237–251, 2007.

[53] J. Błocki, J. Randrup, W. Światecki, and C. Tsang, "Proximity forces," *Annals of Physics*, vol. 105, no. 2, pp. 427–462, 1977.

[54] S. Basu and M. Francoeur, "Maximum near-field radiative heat transfer between thin films," *Applied Physics Letters*, vol. 98, no. 24, p. 243120, 2011.

[55] G. Domingues, S. Volz, K. Joulain, and J.-J. Greffet, "Heat transfer between two nanoparticles through near field interaction," *Physical review letters*, vol. 94, no. 8, p. 085901, 2005.

[56] M. Elzouka and S. Ndao, "High temperature near-field nanothermomechanical rectification," *Scientific Reports*, vol. 7, p. 44901, 2017.